



## **School of Chemistry**

# Fabrication and Characterisation of Boron-Doped Diamond Films Using an ASTeX Microwave Reactor

Ben Robertson

This thesis is submitted in partial fulfilment of the requirements for the Honours  
Degree of MSci at the University of Bristol

Supervisor: **Dr. Neil Fox**

Second assessor: **Professor Paul May**

Third assessor: **Dr. Colin Western**

## Acknowledgements

I would like to thank my primary assessor Dr. Neil Fox and his postdoc Dr. Hugo Dominguez Andrade for their continual input and guidance. I would also like to thank Alex Croot and Gary Wan for their assistance on the microwave reactor and general enquiries, and Dr. Jean-Charles Eloi from the Electron Microscopy department for producing the SEM images.

I extend my gratitude to all the members of the Bristol diamond group, and everyone else involved with the project for their support.

## Abstract

Boron-doped diamond (BDD) is a wide bandgap semiconductor ( $E_{\text{gap}} = 5.47 \text{ eV}$ ) with a wide range of electrical applications. It has superior thermal and electronic properties than any of its analogues which has boosted research during the last 30 years. At present, chemical vapour deposition (CVD) is the most prominent form of diamond synthesis. It occurs *via* the chemical absorption of carbon-containing gas phase molecules onto a substrate surface at high temperature (700 – 1000°C) and low pressure (~0.1 atm). There are many types of CVD reactors, each with their own advantages and disadvantages, but there is a lack of characterisation for BDD film growths in these reactors in the CVD diamond industry, while demand for higher accuracy diamond films rises. Important properties that require better control include: film thickness; surface morphology; and conductivity.

The objective in this thesis is to begin to characterise film growth in the ASTeX plasma-enhanced microwave (PEMW) reactor by conducting a growth calibration experiment using a range of standard growth parameters. It was found that the growth rate of heavily boron-doped diamond remains constant for 10 hours ( $0.72 \mu\text{m}\cdot\text{h}^{-1}$ ) until a change in the growth mechanism leads to a dramatic increase in the rate, reaching  $4.13 \mu\text{m}\cdot\text{h}^{-1}$ .

In the final part of this thesis, the effect of boron contamination in the reaction chamber is examined. For some of BDD's applications, layers of varying boron contents are required to alter the electron transport mechanism through the film. Typically, a multi-chamber process is used to grow these layers as the residual boron from previous growths can be recycled into subsequent growths. Switching out the reaction chamber is laborious; however, it is possible to grow lightly doped films with the residual boron in a contaminated chamber hence the aim here is to quantify the depletion of boron for successive growths in the chamber, and whether the depletion corresponds to a drop in the conductivity which is measured using the van der Pauw method.

The quality of all the films produced in this study were analysed using Raman spectroscopy, and the high-quality films will likely be used in further studies in the Bristol diamond group.

## Contents

Acknowledgements .....	2
Abstract .....	3
1 Introduction .....	5
1.1 Diamond Growth.....	6
1.1.1 CVD Diamond Growth .....	6
1.1.2 CVD Reactors .....	11
1.1.3 Doping .....	13
1.2 Diamond as a Semiconductor .....	15
1.2.1 P-N Junctions .....	16
1.2.2 Schottky and Ohmic Junctions.....	18
1.3 Secondary Electron Emission .....	20
1.3.1 Reflective and Transmissive dynode structures in PMTs .....	22
2 Experimental Methods .....	26
2.1 The MW PECVD Reactor.....	26
2.2 Sample Fabrication.....	28
2.2.1 BDD.....	28
2.2.2 RBDD.....	29
2.3 Scanning Electron Microscopy .....	30
2.4 Raman Spectroscopy.....	30
2.5 Van der Pauw Setup .....	31
2.6 Secondary Ion Mass Spectrometry .....	31
3 Results and Discussion .....	32
3.1 BDD Growth Calibration.....	32
3.1.1 SEM Images .....	32
3.1.2 Raman.....	33
3.1.3 Growth Rate Analysis .....	34
3.1.4 Grain Size Analysis.....	37
3.2 RBDD Experiment.....	39
3.2.1 Raman.....	39
3.2.2 VDP .....	42
3.2.3 SIMS.....	43
4 Conclusions .....	44
5 Future work.....	44
References .....	45

# 1 Introduction

Diamond exhibits a range of extreme properties, it is the hardest known natural material and has the highest thermal conductivity of any material at room temperature<sup>1</sup> which makes diamond a hugely sought-after gemstone for its extensive use in industrial processes such as cutting and mechanical machining. Unfortunately, natural diamond is very rare and costly and often found with impurities which has previously hindered much research until the invention of synthetic diamond routes in the early 1900s.<sup>1</sup>

Diamond synthesis by the high-pressure, high-temperature (HPHT) catalytic process<sup>2</sup> and chemical vapor deposition (CVD)<sup>3</sup> have been responsible for its commercial use in numerous engineering applications. Desired properties, such as electron mobility and doping, can be fine-tuned in these synthesis routes which is important for its applications.<sup>4</sup>

Synthetic diamond produced by CVD has tremendous applications in electronic devices due to its exceptional electronic and thermal properties. Diamond is a wide bandgap semiconductor ( $E_{\text{gap}} = 5.47$  eV) but it behaves as an insulator at room temperature. Its properties potentially enable devices that are beyond the scope of current systems in terms of operating frequency, power handling capacity, operating voltage, and operating environment.<sup>5</sup>

## 1.1 Diamond Growth

The first reproducible synthetic diamond was made in 1955 by General Electric. The idea was to replicate the conditions of diamond formation in the Earth's mantle by employing high pressure and high temperature on graphite *via* a catalytic reaction.<sup>6</sup> The Gibbs free energy for the conversion of graphite to diamond is a small positive value (+40.6 kJmol<sup>-1</sup>) at 25°C, 1 atm,<sup>7</sup> which means diamond is a metastable allotrope of carbon; however, the conversion of graphite to diamond is extremely slow at ambient conditions. Therefore, high temperatures and pressures of around 1500°C and 5 GPa respectively, often with a metallic solvent catalyst, is required to feasibly reach the activation energy for the conversion.<sup>8</sup> This research led to the development of the so called high-pressure high temperature (HPHT) method.

Furthermore, HPHT is a slow and costly synthetic route, limited to producing small (1 cm<sup>3</sup>) single crystals which limits its range of applications.<sup>6</sup>

Today, chemical vapour deposition is the most prominent form of diamond synthesis. It occurs *via* a gas phase reaction above a heated substrate, followed by the chemical absorption of the active gas molecules onto the substrate surface. The gas phase is usually a mixture of CH<sub>4</sub> and H<sub>2</sub> pumped into a vacuum chamber which, under a unique set of conditions, will deposit sp<sup>3</sup> carbon one atom at a time onto the substrate forming the tetrahedral diamond structure.<sup>9</sup>

### 1.1.1 CVD Diamond Growth

The conditions which diamond will grow during CVD is dependent on the gas phase mixture and the temperature of the substrate. In the 1960s, it was discovered that the presence of atomic hydrogen during the deposition process would lead to the preferential etching of sp<sup>2</sup> graphite, rather than sp<sup>3</sup> diamond, which means more graphite is readily stripped away, leaving behind pure diamond.<sup>10</sup> It could also lead to increased activation of precursor gas molecules (usually CH<sub>4</sub>) in the gas phase.<sup>11</sup> In 1991, Bachmann *et al.* amassed the data from over 70 such deposition experiments and came up with a C-H-O phase diagram (Figure 1.1) showing only a small region where diamond growth is feasible.<sup>11</sup>

In all of Bachmann's experiments, complex chemical reactions in the gas phase take place above a heated substrate. Diamond growth was only observed when the gas composition was in a small region above the CO tie-line which implies that diamond will only grow at certain ratios of gasses in the gas phase mixture, more specifically, when there are low concentrations of precursor gas in excess hydrogen (usually 1% volume CH<sub>4</sub> in H<sub>2</sub>). In a typical CVD reactor, the complex gas phase chemistry above a heated substrate occurs so rapidly that the reactant gasses are instantly broken down into smaller, more reactive components. Hydrogen and methane form excited states in a plasma that can react with and bind onto a substrate surface. Recent speculation suggests that a high concentration of atomic hydrogen plays a critical role in many main processes that take place which supports Bachmann's C-H-O phase diagram (Figure 1.1).<sup>9</sup>

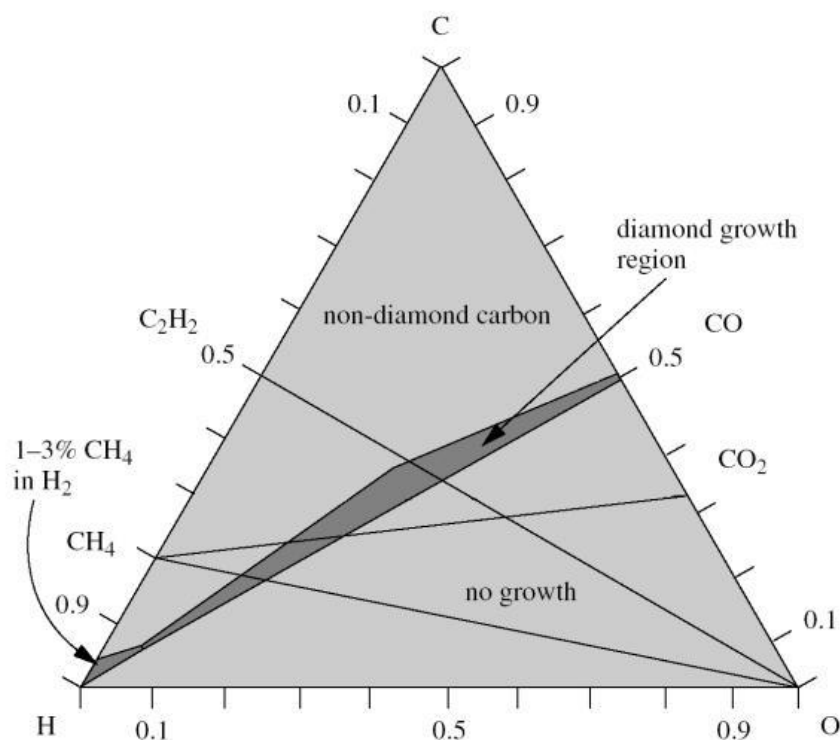


Figure 1.1. Bachmann C-H-O composition triangle reproduced from reference 9. There is a small region of growth above the C-O tie line. The growth conditions in this study are mainly methane in hydrogen (small region on the left).

It has been suggested that in CVD systems containing oxygen or OH species in the plasma, the OH radicals behave similarly to H atoms in that they etch non-diamond carbon from the surface of the film and remove unsaturated hydrocarbons from the gas phase. Higher growth rates and better-quality films have been reported for oxygen-containing systems suggesting that the OH radical is more effective at etching than the H atom. The use of CO<sub>2</sub>/CH<sub>4</sub> gas mixtures in microwave plasma CVD has also been reported to enable growth at lower temperatures.<sup>12</sup>

Further studies about the gas phase have revealed that the addition of oxygen to halocarbon-hydrogen systems (CF<sub>4</sub>/H<sub>2</sub>, CCl<sub>4</sub>/H<sub>2</sub>, CCl<sub>2</sub>F<sub>2</sub>/H<sub>2</sub> and CH<sub>3</sub>Cl/H<sub>2</sub>) can enhance the growth rate.<sup>10</sup> Studies using atomic hydrogen actinometry showed that the presence of a halogen is responsible for an increase in atomic hydrogen concentration and that the addition of oxygen to these halogenated systems increases the carbon solubility in the gas phase.<sup>13</sup>

In all CVD diamond experiments, there are 3 main steps that are necessary to establish diamond: a) seeding; b) nucleation; and c) growth.

#### a) Seeding

Diamond seeding describes the pre-treatment of a substrate to allow polycrystalline diamond to grow effectively. Diamond films will only grow on, and adhere to, substrates that are able to form a surface carbide layer, such as Si, W and Mo, however the reactivity of a substrate cannot be too high otherwise

carbon will dissolve into it stopping the growth.<sup>9</sup> Furthermore, the substrate should withstand temperatures of 700-1000°C as the temperature of the substrate during growth is usually above 700°C to ensure the formation of polycrystalline diamond rather than amorphous carbon. Silicon wafers are a common choice because they are cheap, bind well with carbon, and are structurally weaker so they are easy to etch away.

To speed up nucleation, these substrates can be treated with a diamond nanoparticle solution in a process known as seeding. Diamond nanoparticles are deposited on the substrate surface providing nucleation sites for growth to begin.

## b) Nucleation

As previously mentioned, atomic hydrogen is a key component for the etching of diamond as it is involved in essential chemical reactions at the diamond-gas interface. It is formed by the reversible dissociation of molecular hydrogen in the highly active gas phase. It can then go on to either react with other species in the gas phase, including the carbon-containing precursor molecules to activate them (e.g.  $\text{H} + \text{CH}_4 \rightarrow \text{H}_2 + \text{CH}_3$ ), or etch the diamond surface.<sup>10</sup> Figure 1.2<sup>9</sup> shows a simplified mechanism of the surface etching followed by the addition of  $\text{CH}_3$ .

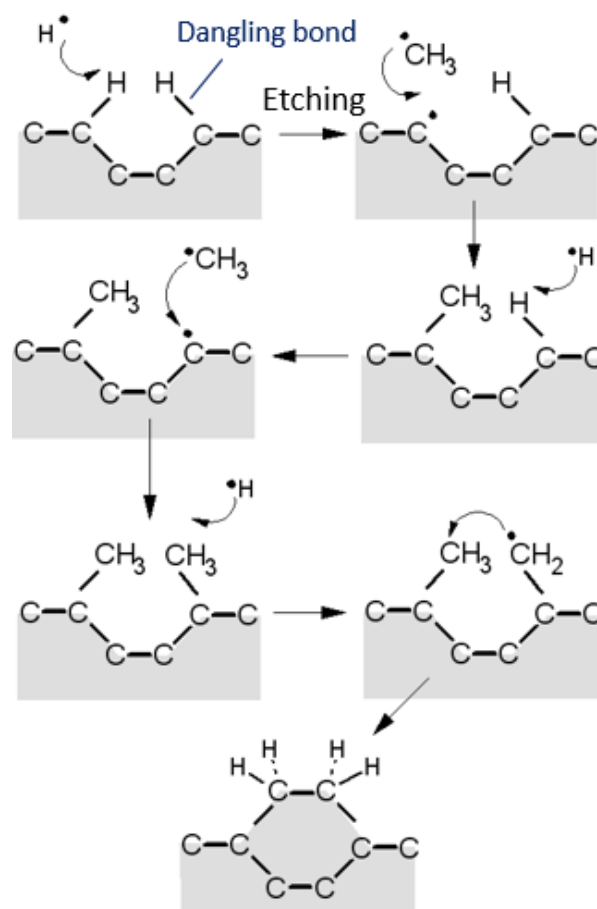


Figure 1.2. A proposed schematic of the stepwise addition of  $\text{CH}_3$  to a diamond surface. The first step is the etching of a dangling bond by atomic hydrogen.<sup>6</sup>

Growth will begin at a nucleation site where  $sp^3$  diamond bulk is surface terminated with H (or sometimes OH for oxygenated systems). There is an equilibrium of thermal desorption and re-adsorption of molecules at the diamond surface. The presence of atomic H helps stabilise the diamond lattice by quickly bonding to any excess dangling bonds thus preventing any cross linking and subsequent graphitisation.<sup>14</sup> Occasionally, a  $CH_3$  molecule will chemically adsorb to an etched dangling bond which, *via* a series of partially understood chemical reactions, will lead to slow diamond growth (Figure 1.2).

Other functions of atomic hydrogen include the breakdown of long chain hydrocarbons into smaller, more relevant species, and the removal of graphitic clusters from the surface of the diamond film as atomic hydrogen is known to etch  $sp^2$  graphitic carbon faster than  $sp^3$  diamond.<sup>9</sup>

### c) Growth

Once the diamond seeds have been nucleated on the non-diamond substrate, heteroepitaxial growth occurs across the surface until the individual crystals come into contact. This forms the seeding layer highlighted in Figure 1.3. After this point, columnar growth proceeds upwards.

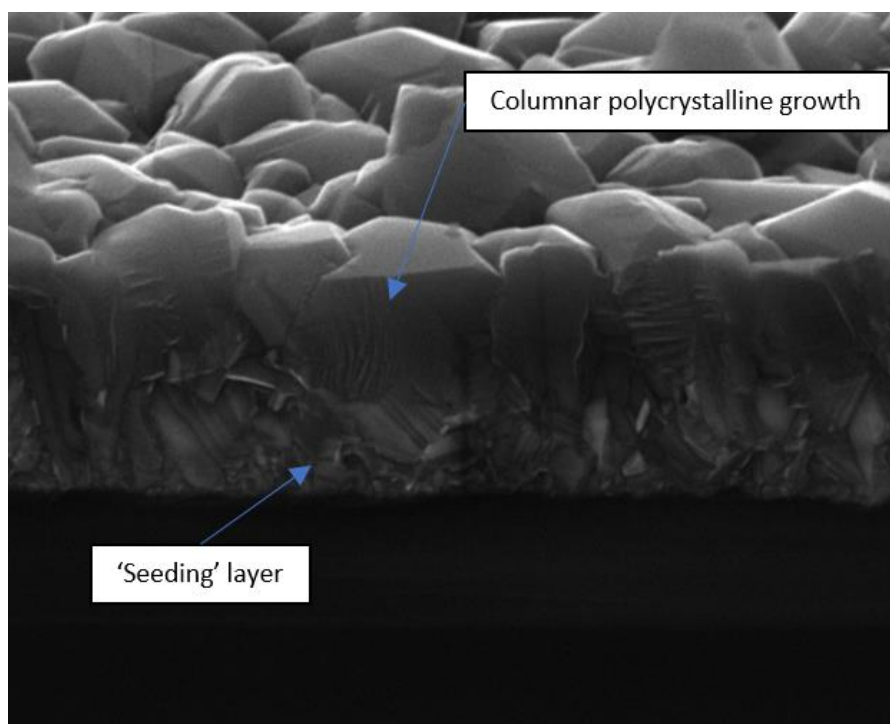


Figure 1.3. An example of boron-doped diamond grown for 4 hours, 2.5  $\mu\text{m}$  thick. Image produced by SEM.

The seeding layer is composed of randomly orientated crystals and has a slow growth rate ( $< 1 \mu\text{m}\cdot\text{h}^{-1}$ ) compared to polycrystalline growth ( $4\text{-}10 \mu\text{m}\cdot\text{h}^{-1}$ ). This effect will always be seen when diamond is grown on a non-diamond substrate.<sup>15</sup>

The surface morphology (defined as texture and grain size) is an important feature of these thin films as their desired chemical properties for their applications are normally determined at the surface. For example, highly orientated large grained crystals are good for heat conducting layers, while rough

(111) surfaces are good for electron emission.<sup>16</sup> The surface morphology largely depends on the relative growth rates of the different crystal planes that arise and, for the early stages of growth, the surface morphology of the nucleation seed. On the surface of these planes are facets of varying shapes, defined by the Miller index system e.g. square (100), triangle (111) (Figure 1.4). Different facets have different growth velocities from them which is influenced by the temperature and gas phase composition.

The surface morphology can be characterised by an  $\alpha$ -parameter (Equation 1) which is the ratio of growth rates in the (100) direction to the (111) direction.

$$\alpha = \sqrt{3} \frac{v_{(100)}}{v_{(111)}} \quad (1)$$

Experimentally, the  $\alpha$ -parameter is determined by the visualisation of each crystals deviation from the perfect cubo-octahedron obtained at  $\alpha = 2$  (Figure 1.4) and is averaged over several crystals.<sup>17</sup>

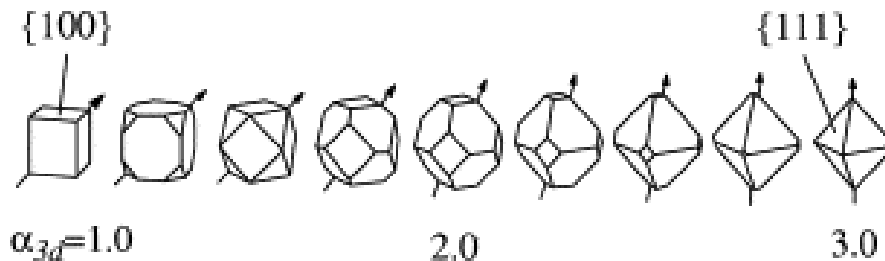


Figure 1.4. Idiomorphic crystal shape. The cubo-octahedron shape ( $\alpha = 2$ ) is conceptually obtained from the continuous change from a cube to an octahedron. Reproduced from reference 17.

Growth errors, such as stacking faults, can sometimes lead to phenomena known as twinning. Twinning is a non-geometric rotation from the parent lattice resulting in five-fold symmetry crystal shapes such as icosahedra (Figure 1.5, top) and decahedra (Figure 1.5, bottom) which are often found as single particles, or embedded in closed layers.<sup>18</sup> It is also shown that the basic morphology of a multiply twinned particle (MTP) is determined at the early part of the nucleation phase, i.e. when growth propagates from the adsorbed nanoparticle seeds.<sup>19</sup> MTPs are characteristic of boron-doped diamond and effects the growth rate and the conductivity of the sample. Twinning is characteristic of boron-doped diamond and causes the growth rate of diamond to reduce significantly.

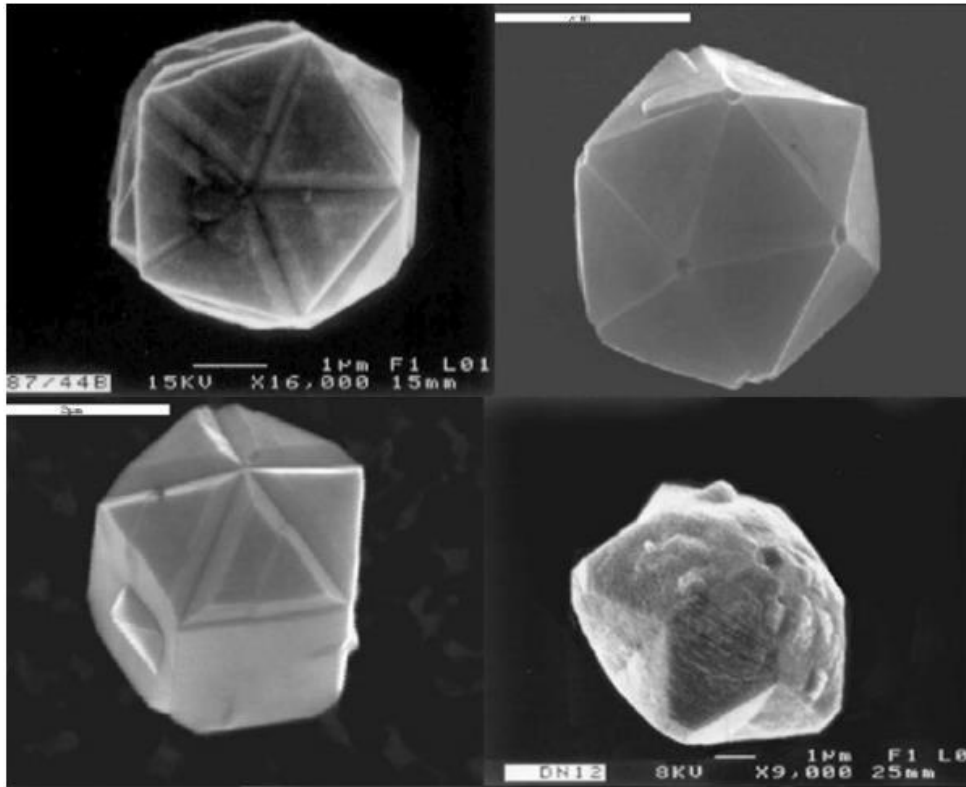


Figure 1.5. Icosahedra (top row) and decahedra (bottom row) diamond crystals grown at different growth condition, all with alpha-parameter  $1 < \alpha < 2.5$ . 5-fold symmetry shapes arise as a result of twinning. SEM images reproduced from reference 18.

### 1.1.2 CVD Reactors

In CVD synthesis, there are 3 known ways to activate the precursor molecules and hence there are 3 types of CVD reactors for growing polycrystalline diamond. These activation methods utilise thermal methods (e.g. a hot filament), electric discharge (e.g. DC, RF or microwave plasma), or a combustion flame.

The use of CVD systems was first popularised in the 1980s by the Japanese NIRIM (National Institute for Research in Inorganic Materials) who consolidated prior articles to give detailed techniques for hot filament (HF) and microwave (MW) CVD.<sup>20</sup>

The HFCVD technique involves heating a filament (usually tungsten, tantalum or rhenium) to  $> 2000^{\circ}\text{C}$  very close to the heated substrate surface. The gas mixture is pumped in at typical flow rates of  $10 - 100 \text{ cm}^3 \text{ min}^{-1}$  and showers over the hot filament producing the active species for growth. Because of its high flexibility and ability to grow thick films, it is the technique of choice for the deposition on cutting tools.<sup>21</sup> However, the hot filament can contaminate the sample which reduces its quality. The hot filament is also susceptible to oxidation and corrosion from gas mixtures containing oxygen and halocarbons respectively and therefore, it is not the preferred technique for electronic and optical applications.<sup>9</sup>

Although more expensive, MWCVD is the more established technique due to the increased deposition rate, and the quality of films produced. Here, microwave power is coupled into the reaction chamber,

with the substrate already loaded, to create a discharge that strikes a plasma. In this process, electrons are accelerated within the oscillating electric field produced by the microwaves, and transfer their energy to the gas mixture through collisions generating the active species *via* dissociations.<sup>22</sup> The microwaves are directed such that they constructively interfere just above the loaded substrate so that the active gas molecules can easily deposit on the substrate surface. The geometry of the chamber is important for reproducibility as it strongly influences the extent and location of the microwave discharge.<sup>20</sup>

The NIRIM-type (Figure 1.6a) reactor was the first microwave reactor produced in 1982. In this simple configuration, a quartz discharge tube is inserted through a rectangular waveguide to allow the propagation of 2.45 GHz microwaves.<sup>12</sup> There are some disadvantages with this configuration which led to the development of alternative reactor designs. The drawbacks include: limited plasma size due to the presence of nearby walls, and therefore a limited deposition area; high power plasmas could destroy the discharge tube; and plasma etching of the quartz often lead to Si and O contamination of the diamond.<sup>15</sup>

In 1988, Bachmann *et al* and Smith at ASTeX (Applied Science and Technology) developed the ASTeX-type reactor which uses a silica 'bell jar' shape (Figure 1.6b) instead of a silica tube in the NIRIM-reactor. In this configuration, 2.45 GHz microwaves travel through the waveguide and are coupled into the bell-shaped reaction chamber *via* an antenna.<sup>20</sup> The plasma is generated at the point of highest electric field inside the evacuated quartz bell jar. This technique was improved a few years later; the bell jar shape was replaced by a flat quartz window (Figure 1.6c)<sup>20</sup> which increased the maximum microwave power that could be coupled into the plasma from 1.5 kW to 5 kW. This is the reactor used in this study.<sup>23</sup>

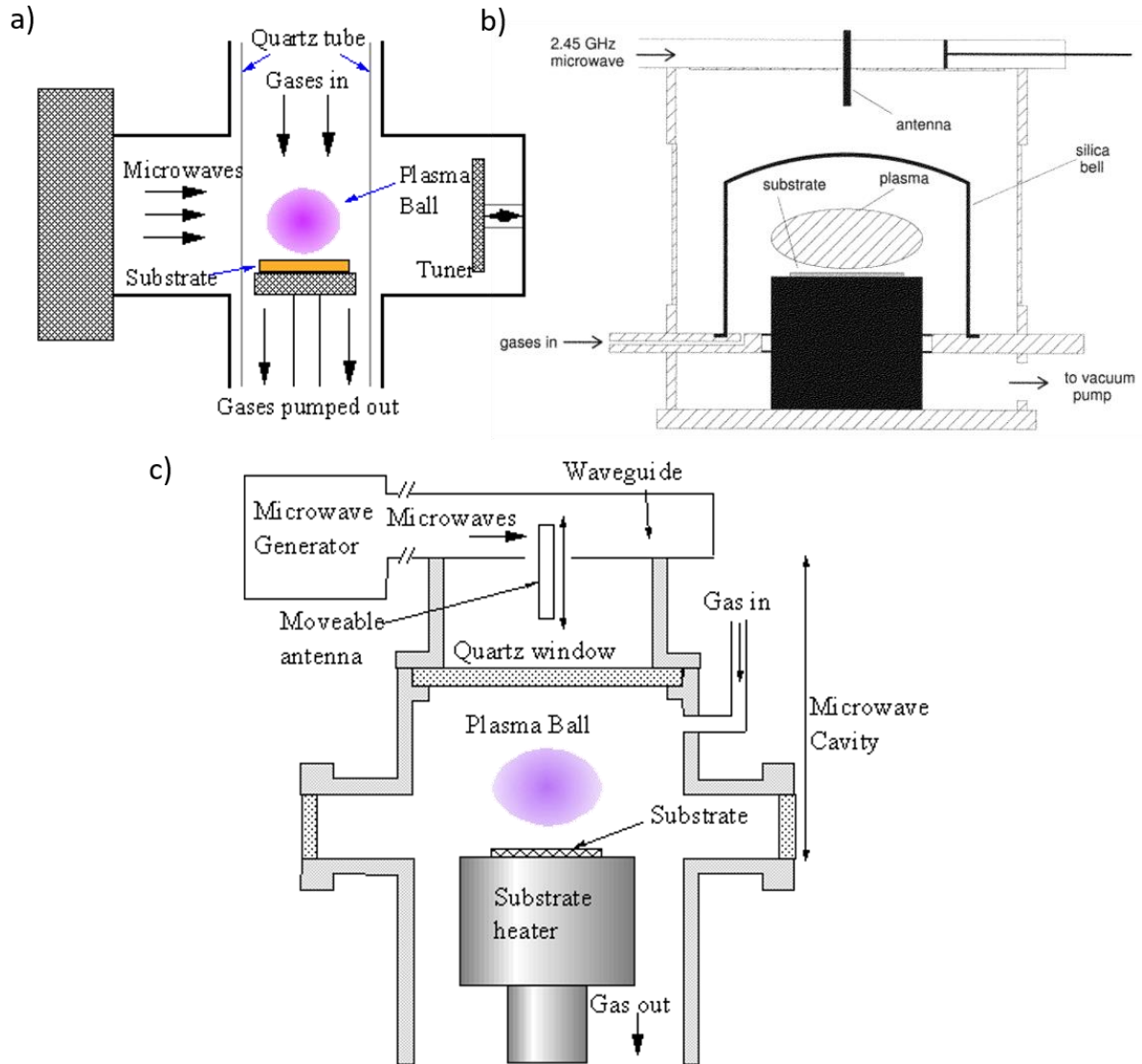


Figure 1.6. Schematics of a) the NIRIM reactor;<sup>15</sup> b) 'bell jar' ASTeX reactor;<sup>20</sup> and c) the modern day conventional ASTeX reactor which will be used in this study.<sup>23</sup>

Unlike the NIRIM reactor, the ASTeX reactor does not contaminate the diamond with Si or O as the waveguide is made of stainless steel instead of quartz. Another advantage is that the substrate temperature can be controlled independently of the microwave power coupled into the system.<sup>12</sup>

### 1.1.3 Doping

The bottom-up, CVD approach to diamond synthesis has proved to be cheaper than HPHT as it uses lower temperatures. Moreover, it allows us to tune properties by altering the growth conditions. For example, doping has enabled the use of diamond in electronic devices as it converts diamond into a p-type, or n-type semiconductor. Intrinsic diamond is an insulator at room temperature as the activation energy required to promote an electron from the valence band to the conduction band is too high. However, the incorporation of impurities, that modify the electronic band structure of

diamond by shifting the Fermi level into the crystal lattice, lowers this energy making the promotion of an electron feasible.

There are two types of doping, negative (n-) type involves the incorporation of atoms with more valence electrons than carbon, thus donating free electrons to the crystal lattice providing the activation energy can be met (Figure 1.7). Nitrogen very easily adsorbs to diamond during growth *via* ring opening mechanisms.<sup>24</sup> However, the activation energy required to promote the free electron to the conduction band is still very high (1.7 eV).<sup>25</sup> Shallow donors (such as P, O, and As) have lower ionisation energies,<sup>26</sup> but they do not adsorb well to diamond as their ionic radii discrepancy from carbon may stress the lattice and cause defects.<sup>15</sup>

Positive (p-) type doping requires atoms that have fewer valence electrons than carbon, such as boron which incorporates well into the diamond lattice and has a very low activation energy (0.37 eV).<sup>27</sup> The boron chemical bonds can accept an electron from the valence band. When this happens, the hole hops in the other direction to the electron and the positive charge moves.<sup>28</sup>

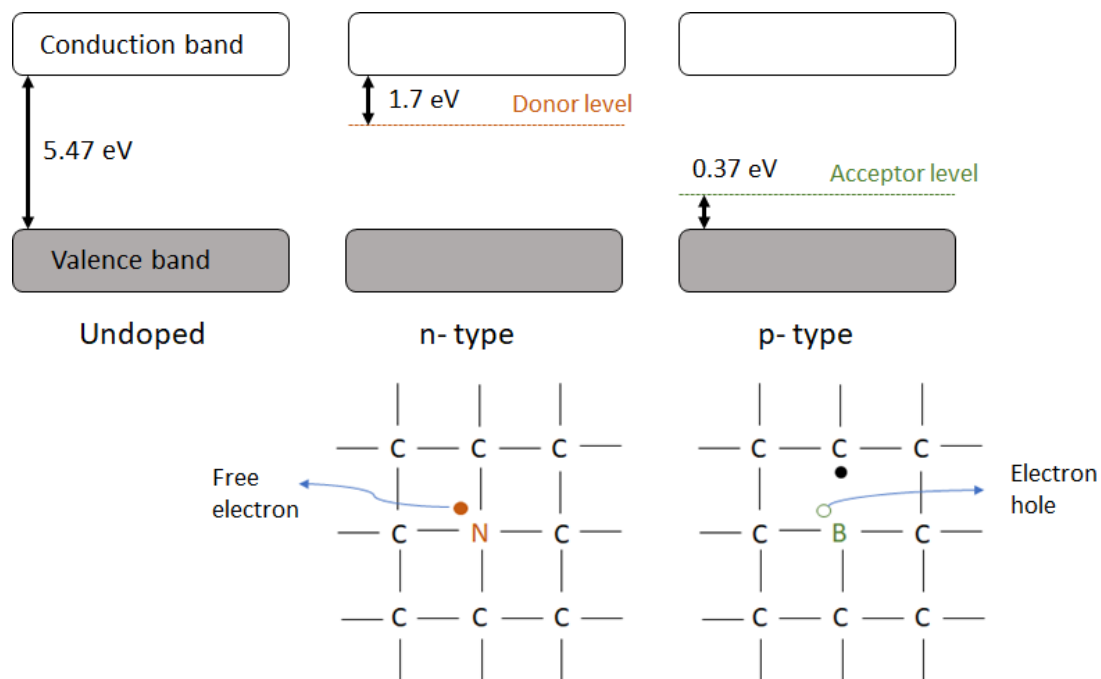


Figure 1.7. The band gaps for undoped and doped diamond (top) and simplified examples of the 2D bonding structure in  $sp^3$  carbon lattices (bottom). n- type dopant shifts the Fermi level towards conduction band, p-type shifts the Fermi level towards valence band.

It is known that Increasing the boron concentration in diamond thin films increases the conductivity.<sup>29</sup> However this will also reduce the rate of growth and the quality of the film as the impurity levels rise.<sup>30</sup> Boron concentrations of  $\sim 10^{17} - 10^{19} \text{ cm}^{-3}$  (atomic density) have been reported for Schottky contacts with metals (see later), and higher concentrations ( $10^{21} \text{ cm}^{-3}$ ) will have a metallic conductivity exhibiting a resistance of  $10^{-3} \Omega$ ,<sup>27</sup> and forms ohmic contacts with metals. Additionally, it has been reported that boron prefers to adsorb onto (111) facets.<sup>31</sup>

## 1.2 Diamond as a Semiconductor

Doping enables the use of semiconducting diamond in electronic devices. One limiting factor for current computer technology is how closely components can be packed onto a silicon chip without causing severe heat management problems. Diamond has excellent thermal properties: single crystal CVD diamond has a thermal conductivity ( $k$ ) of around  $2200 \text{ W}\cdot\text{m}^{-1}\cdot\text{K}^{-1}$  at room temperature making them ideal for handling high powers.<sup>5</sup>

Single crystal CVD diamond also exhibits both the highest electron and hole mobilities at room temperature of any wide-bandgap semiconductor. Mobilities of  $4500 \text{ cm}^2\cdot\text{V}^{-1}\cdot\text{s}^{-1}$  for electrons and  $3800 \text{ cm}^2\cdot\text{V}^{-1}\cdot\text{s}^{-1}$  for holes have been reported in intrinsic diamond at room temperature.<sup>32</sup> Scattering induced by elevated levels of impurities causes the mobility to drop with increasing dopant concentration. In the case of boron-doped diamond (BDD), the measured hole mobility drops from  $1500 \text{ cm}^2\cdot\text{V}^{-1}\cdot\text{s}^{-1}$  at  $[B] \approx 5 \times 10^{16} \text{ cm}^{-3}$ , to  $450 \text{ cm}^2\cdot\text{V}^{-1}\cdot\text{s}^{-1}$  at  $[B] \approx 10^{19} \text{ cm}^{-3}$ .<sup>33</sup> Thus, diamond can exhibit good hole mobility even at high boron concentrations.

In strong electric fields, such as in field-effect transistors, the semiconductor is said to be in a state of velocity saturation and the conductivity is determined by the saturation velocity rather than carrier mobility.<sup>5</sup> The saturation velocity ( $v_s$ ) is given by the equation:

$$v_s = \sqrt{\frac{8E_{opt}}{3\pi m} \tanh\left(\frac{E_{opt}}{2kT}\right)} \quad (2)$$

Where  $m$  is the effective mass of the charge carriers and  $E_{opt}$  is the energy of the optical lattice vibrations, or phonons. BDD has the highest optical phonon energy of any semiconductor ( $E_{opt} = 160 \text{ meV}$ )<sup>33</sup> and thus has a high saturation velocity. According to the literature, the value for the saturation velocity varies between  $1.5 - 2.7 \times 10^7$  for electrons, and  $0.85 - 1.2 \times 10^7$  for holes.<sup>34,35</sup>

These electrical properties make BDD superior to other commonly used wide-bandgap semiconductors. For example, silicon carbide (SiC), which is also used in FETs, has corresponding carrier mobility values of  $900 \text{ cm}^2\cdot\text{V}^{-1}\cdot\text{s}^{-1}$  and  $120 \text{ cm}^2\cdot\text{V}^{-1}\cdot\text{s}^{-1}$  for electrons and holes respectively.<sup>36</sup> SiC reaches similar saturation velocities to BDD, but BDD has an advantage in that it can reach its saturation velocity in fields as high as  $\sim 10 \text{ kV}\cdot\text{cm}^{-1}$ .<sup>5</sup>

Semiconductors form potential barriers at interfaces with metals and other semiconductors. There are two types of interfaces: a metal-semiconductor junction (between a metal and either a p-, or n-type semiconductor), and a p-n junction (between a p- type and an n- type semiconductor). In all semiconductor junctions, charge carriers migrate from the bulk to the interface causing the electronic band structure to bend, upwards for p- doped materials and downwards for n- doped. The Fermi level however does not bend and instead aligns with Fermi-level of the second material *via* charge transfer.

### 1.2.1 P-N Junctions

Figure 1.8 shows a typical P-N junction where a potential difference, or built-in potential ( $\phi_{bi}$ ) prevents charge carriers from freely jumping across the junction however, because of random thermal energy, some electrons will pass across the P-N junction merging with holes on the other side. This is referred to as recombination. The n- type material is thus losing electrons near the surface resulting in a positive charge and equally, the p- type material gains electrons resulting in a negative charge. The end result of recombination therefore is an area of depleted carriers, or depletion region, which has a net zero charge.<sup>37</sup>

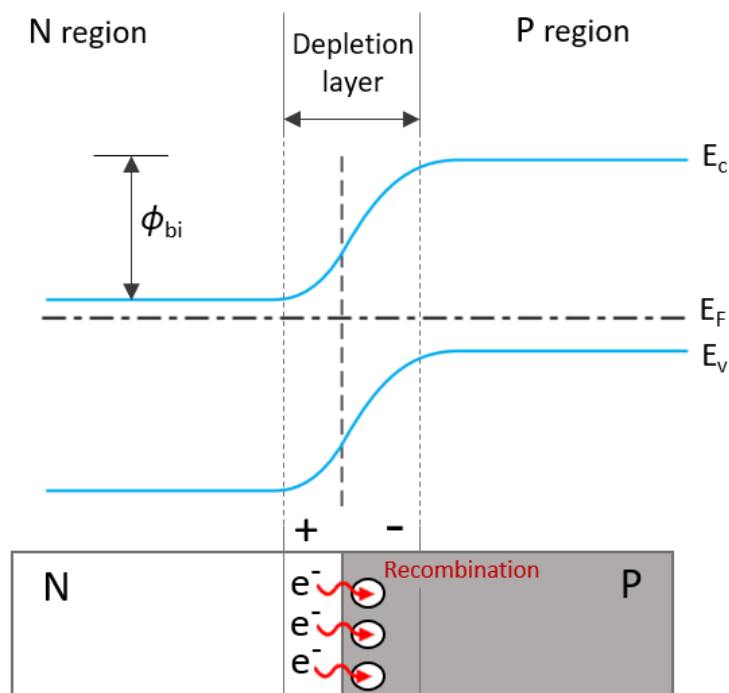


Figure 1.8. Band structure at a P-N junction. The valence band ( $E_v$ ) and conduction band ( $E_c$ ) bend at the interface due to space charge effects, and the Fermi levels ( $E_f$ ) align. Below shows the recombination of electrons and holes at the interface due to thermal fluctuations forming a depletion zone in each material.

In order for current to flow, electrons must overcome the built-in potential ( $\phi_{bi}$ ) which can be done using an external power source as shown in Figure 1.9: this is referred to as biasing. A bias can be applied in both directions which will either aid or oppose the barrier potential. Forward biasing is when a voltage is applied to a P-N junction such that the positive side is connected to the p- type which enables current to flow more easily (Figure 1.9a). The power supply provides an abundance of free electrons that move as conduction band electrons in the N material and valence band electrons in the P material. The depletion region consequently narrows as charge carriers in both materials are forced towards each other.<sup>38</sup>

Conversely, reverse biasing strengthens the barrier potential. The negative terminal of the power supply is connected to the P material which widens the depletion region. Current flow is minimal as electrons in the N material are attracted to the positive terminal, and holes in the P material are pulled in the opposite direction further inhibiting electron flow (Figure 1.9b). If the reverse current is high

enough, current will increase dramatically causing the junction to breakdown. This is known as the breakdown voltage which, if reached, can destroy a device. Zener diodes however operate in the breakdown region. If the current is limited to a reasonable value by the external circuit so that heat dissipation in the P-N junction is not excessive, the P-N junction can be operated in reverse breakdown safely.<sup>37</sup>

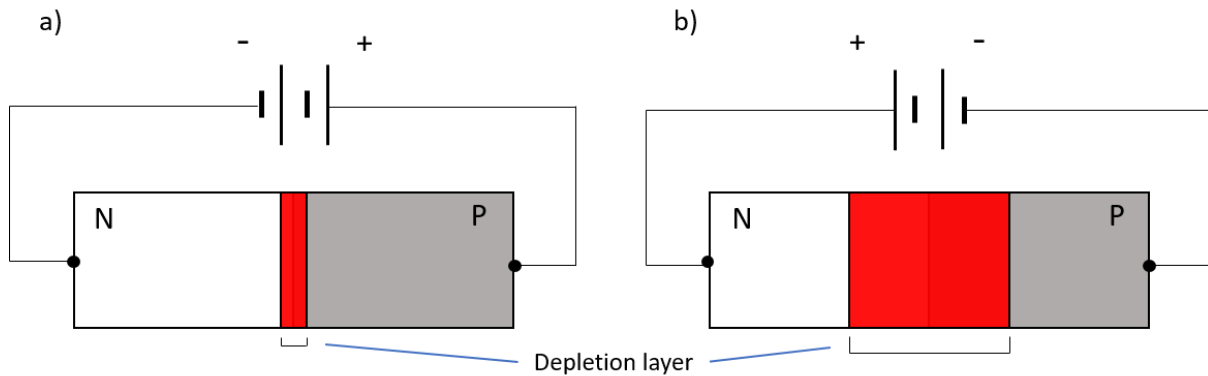


Figure 1.9. Two P-N junctions with a) a forward bias applied allowing electrons to overcome the barrier potential, and b) a reverse bias which inhibits the flow of electrons.

P-N junctions are therefore considered rectifying junctions due to its forward and reverse bias behaviour (Figure 1.10a). The significance of a rectifying junction is that it can convert alternating current to direct current.

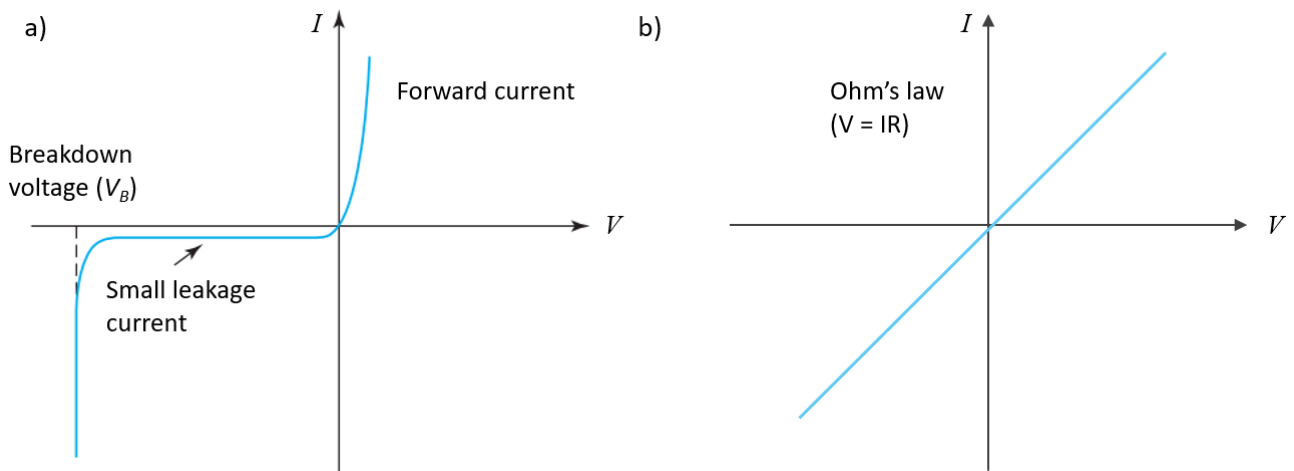


Figure 1.10. a) A rectifying IV curve showing an exponential increase in current when a forward voltage is applied and a breakdown voltage when a reverse voltage is applied. b) A non-rectifying IV curve showing an ohmic relationship.

Additionally, the P-N junction has enabled the studying of the depletion layer, the quasi-equilibrium boundary condition, and other tools and concepts that are important to the understanding of transistors.

### 1.2.2 Schottky and Ohmic Junctions

Metal-semiconductor contacts behave slightly different to P-N junctions: there is no depletion region in the metal and the band bending in the semiconductor is independent of the metal, even for large variations of the work function. This is known as fermi-level pinning.<sup>39</sup> There are two types of metal-semiconductor junctions: a metal with a lightly doped semiconductor (otherwise known as a Schottky diode), and a metal with a heavily doped semiconductor (forming ohmic contacts).

In Schottky diodes, the main current transport process is thermal emission over the potential barrier (in contrast to P-N junctions where recombination is the main electron flow process), or the Schottky barrier height ( $\phi_B$ ).  $\phi_B$  is characterised differently for metal contacts with n- type ( $\phi_{B,n}$ ) and p- type ( $\phi_{B,p}$ ) semiconductors as shown in Figure 1.11a and Figure 1.11b respectively.<sup>40</sup> Charge carriers move through the conduction band in n- type, and the valence band in p- type material, thus their summation is always the band gap energy ( $E_g = \phi_{B,n} + \phi_{B,p}$ ).

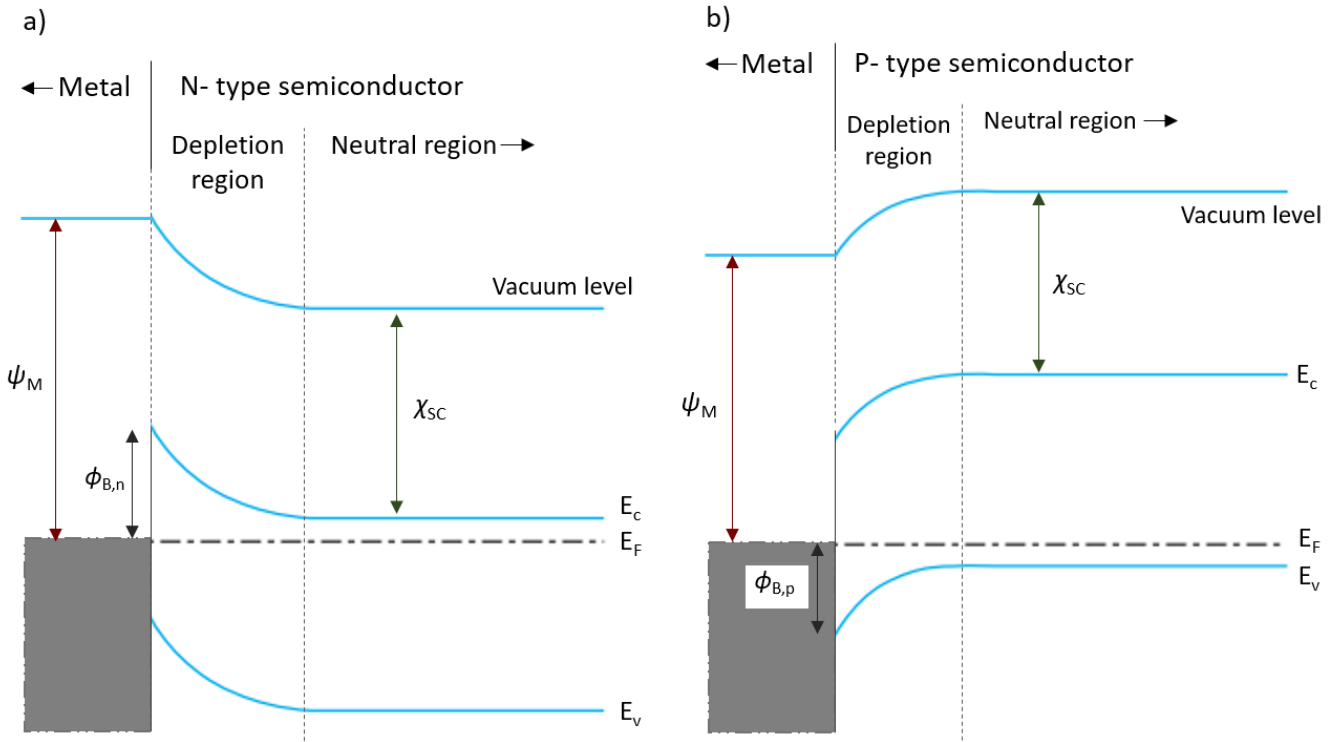


Figure 1.11. Schottky contacts between a metal and: a) an n-type semiconductor; and b) a p-type semiconductor. Where the work function ( $\psi$ ) is the difference between the fermi level ( $E_F$ ) and the vacuum level, and the electron affinity ( $\chi$ ) is the difference between conduction band ( $E_c$ ) and the vacuum level.

For metal – p- type semiconductor contacts, the work function of the metal is less than the work function of the semiconductor ( $\psi_M < \psi_{SC}$ ) and conversely for n- type ( $\psi_M > \psi_{SC}$ ). According to the Schottky-Mott rule, the Schottky barrier height varies with the choice of metal (Equation 3).

$$\phi_{B,p} = E_g + \chi_{SC} - \psi_M \quad (3)$$

A low work function metal provides a low Schottky barrier height for electrons in n- type dopants,  $\phi_{B,n}$ , and a large barrier height for holes in p- type dopants,  $\phi_{B,p}$ . The electron affinity ( $\chi_{SC}$ ) and band gap energy ( $E_g$ ) are both constant for a given semiconductor.

Schottky diodes exhibit similar rectifying characteristics as P-N junction (Figure 1.10a) but have much larger reverse saturation currents. Ohmic contacts follow Ohm's law ( $V = IR$ ) as shown in Figure 1.10b. They generally operate with low-resistance and are critical for the performance of high current devices. The main electron transport mechanism for an ohmic contact is mechanical quantum tunnelling (Figure 1.12) whereby electron waves pass through the Schottky barrier height. Electron waves will emerge from the barrier as a travelling wave again but with reduced amplitude. There is a finite probability that electrons will tunnel through a potential barrier.<sup>40</sup>

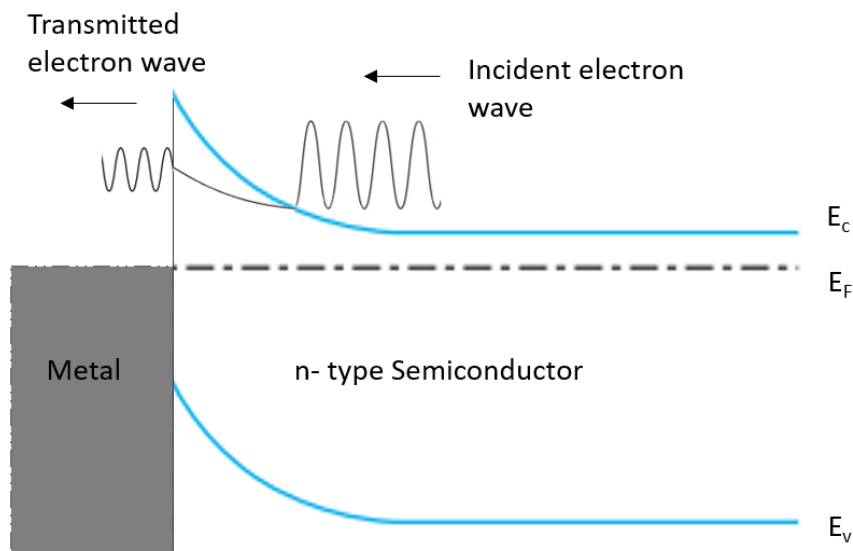


Figure 1.12. Quantum tunnelling graphic, showing an incident electron wave tunnelling through a potential barrier in a metal – n- type Schottky junction.

The tunnelling probability increases exponentially with decreasing barrier thickness, which depends primarily on the Schottky barrier height – dependant on the metal and semiconductor as shown in Equation 3 – and the extent of band bending. Band bending is a result of charge imbalance at the interface of any type of junction. The probability of tunnelling becomes extremely high as band bending increases. This can be done by increasing the dopant concentration e.g.  $[B] > 10^{19} \text{ cm}^{-3}$  forms ohmic contacts in BDD. The physical interpretation of band bending can be thought of as the electrostatic energy experienced by an electron as it moves through the interface.<sup>40</sup> As the electron in the semiconductor experiences repulsion from the negatively charged Helmholtz layer located in the metal, its potential energy rises, and the bands bend upward, and vice versa for p- type semiconductors.<sup>41</sup>

As discussed, diamond behaves as an insulator at room temperature but when doped with boron, it forms a p-type semiconductor with excellent electrical and thermal properties. Since this discovery, diamond contacts forming P-N junctions and Schottky diodes have been researched extensively. The type of contact formed can be altered by the extent of boron doping in the sample as this directly effects the conductivity. This study aims to fabricate thin boron-doped diamond films appropriate for applications in dynodes (utilising its secondary electron emission properties), and long-lifetime nuclear batteries.

### 1.3 Secondary Electron Emission

Secondary electron emission (SEE) was discovered by Austin and Starke in 1902 who found that metals were able to emit a larger numbers of electrons than it was receiving.<sup>42</sup> It occurs when a solid surface is bombarded with incident (primary) charged particles, such as ions or electrons, and secondary electrons are emitted. A material's ability to produce secondary electrons is characterised by the secondary emission yield (SEY),<sup>43</sup> which is the number of secondary electrons emitted per primary particle (Equation 4), and the energy distribution of the emitted electrons. A good secondary electron emitter will have a high SEY ( $\delta$ ) with a low energy distribution. Materials with high SEY are useful for electron multiplication and signal amplification devices such as photomultiplier tubes.<sup>44</sup>

$$\delta = 1 - \frac{I_T}{I_p} \quad (4)$$

where  $I_T$  is the total output current and  $I_p$  is the incident, primary electron current. The true secondary current cannot be measured directly, so the total output current is used instead which is the sum of the primary and secondary electron currents ( $I_T = I_p + I_s$ ).<sup>45</sup>

The generation of a secondary electron occurs after a collision event between a primary electron and an electron in the valence band of the material. This transfer of energy promotes the electron to the conduction band, creating an electron-hole pair which can only happen in a certain energy range of the primary electron. For a valence electron to be promoted, it must absorb roughly three times its band gap energy from the primary electron. This gives a value of 16.4 eV for diamond, and 19 eV for polycrystalline diamond.<sup>46</sup>

Once generated, a secondary electron can gain kinetic energy through collisions with primary electrons or lose energy by creating additional electron-hole pairs or colliding with phonons. In order for a secondary electron to escape and generate a current, it must reach the surface with a high enough energy to overcome the surface potential. This is shown to be more feasible for insulators/semiconductors than it is for metals due to differences in energy loss and escape processes.

In metals, internal secondary electrons primarily lose their energy through electron-electron collisions, or electron scattering as there are many electrons in the free-flowing conduction band. Energy can also be lost through collisions with phonons and defects. For a secondary electron to escape a metal, its energy must exceed the sum of the Fermi level and the work function ( $\psi_M + E_F$ ); this minimum escape energy is typically  $\sim 10$  eV which results in a small SEY for metals.<sup>47</sup>

In insulators and semiconductors, the minimum escape energy over the vacuum barrier is the electron affinity ( $\chi$ ) which is typically  $\sim 1$  eV. Internal secondary electrons (that have been previously generated) with energy higher than  $E_{\text{gap}}$  can excite valence band electron creating additional electron-hole pairs. Otherwise, the main energy loss mechanism is through electron-phonon and electron-impurity collisions. Therefore, the absence of electron scattering gives insulators a high SEY. For example,  $\delta_{\text{max}}$  is 6.8 for NaCl, and 25 for single crystal MgO.<sup>47</sup> However, assuming more secondary electrons are emitted than primary electrons arriving, there is a net electron flow from the sample to the vacuum and some level of electrical conductivity is required to replenish the lost electrons. Insulators have no conductivity and experience sample charging which will decrease the SEY to 1 over a period of time.<sup>47</sup> Charge build-up effects can be reduced in practice by making the material more conductive – boron

doping in diamond is one way to do this. Other ways include coating the high SEY material, such as aluminium oxide ( $\text{Al}_2\text{O}_3$ ), magnesium oxide ( $\text{MgO}$ ), or gallium arsenide phosphide ( $\text{GaAsP}$ ), onto a conducting substrate material such as nickel, stainless steel, or beryllium copper ( $\text{CuBe}$ ).<sup>48</sup>

In diamond, dopants are used to increase electrical conductivity and replenish the electrons lost during secondary emission. Figure 1.13<sup>47</sup> shows the effect of primary electron energy on the SEY for boron-doped diamond and nitrogen-doped diamond. Nitrogen is a deep donor and is therefore an insulator at room temperature. BDD however shows a maximum SEY at  $\sim 900$  eV primary electron energy due to the increased conductivity. The yield decreases with higher values of primary electron energy as the penetration depth of the primaries exceed the escape depth of the secondary electrons.

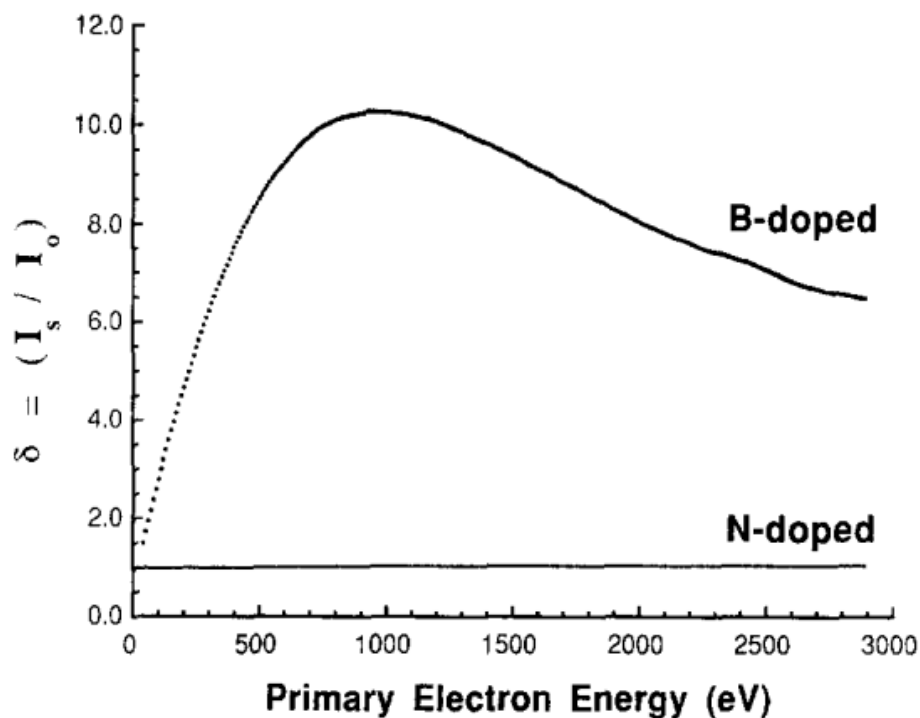


Figure 1.13. Reproduced from reference 47. Effect of electrical conductivity on secondary electron yield from diamond. The boron doped diamond samples used in this study have resistivities between  $50 \Omega\cdot\text{cm}$  -  $170 \text{ k}\Omega\cdot\text{cm}$ .

Primary electrons slow down in materials due to energy transfer processes such as collisions with electrons, or interactions with phonons or defects. Increasing the boron concentration in BDD will increase the frequency of electron-impurity collisions thus reducing the escape depth and SEY.

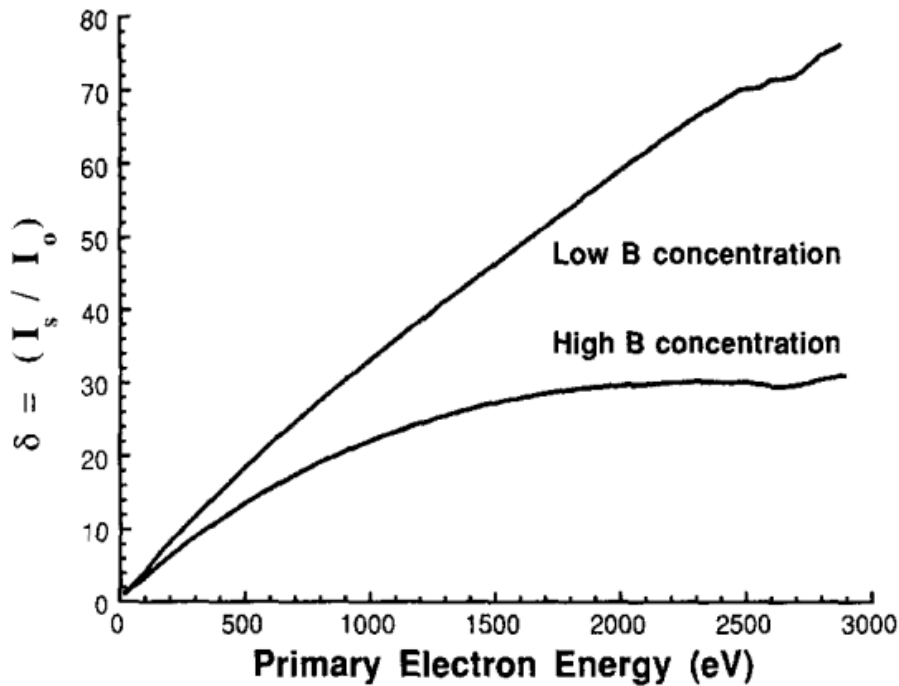


Figure 1.14. Reproduced from reference 47. Effect of boron impurity level on secondary electron yield from diamond. The low [B] samples have resistivity between 50 – 170 k $\Omega$ ·cm, and the high [B] samples have resistivity between 50 – 170  $\Omega$ ·cm.

Higher energy primary electrons generate more secondary electrons and penetrate deeper into a sample. According to Figure 1.14, diamond with lower levels of boron impurity will have a higher SEY at higher primary electron energies than higher [B] because of the increased interactions with lattice defects. Studies show that the generation of these secondary electrons occurs mostly within a small range towards the end of the primary electron's penetration depth as its slower movement gives more time for it to interact with valence electrons.<sup>49</sup> Secondary electrons that originate deeper within the sample however will lose more energy before reaching the surface and are therefore less likely to escape. Secondary electrons have low energy (< 50 eV) and therefore a low escape depth of  $\sim 10$  nm.<sup>47</sup>

### 1.3.1 Reflective and Transmissive dynode structures in PMTs

The SEE ability of BDD has been researched extensively for their application as dynodes used in photomultiplier tubes. A photomultiplier tube converts high energy photons into a current. They are typically constructed with an evacuated glass housing containing a photocathode, several dynodes, and an anode. A high energy photon is converted to a low energy electron at the photocathode which can then produce more electrons as it interacts with the dynode structures (Figure 1.15b). The dynodes are positioned such that the electric fields between them cause the electrons emitted by each dynode to strike the next with an energy of a few hundred eV. PMTs have been perfected in their 70 years of existence and have now reached a quantum efficiency of 43% at 350 nm, close to their theoretical maximum.<sup>50</sup>

Reflective SEE (Figure 1.15a, left) is when secondary electrons are emitted from the same surface the primary electrons bombard. For this to occur, the escape depth of the secondary electrons must

exceed the penetration depth of the primary electrons. Conversely, transmissive SEE (Figure 1.15a, right) is when secondary electrons are emitted from the other side of the incident bombardment leading to a linear propagation of secondary electrons. For this to occur, the sum of the penetration and escape depth must be greater than the material's thickness.

Dynode structures, used in PMTs (Figure 1.15b), can either be reflective or transmissive, with the more recent research emphasis on the latter.<sup>48</sup> Both involve a series of SEE events in which current amplification, or gain, is proportional to power of the supply voltage. Secondary electrons produced at the first dynode structure are accelerated to the next dynode structure by a potential field and the generation of secondary electrons propagates.

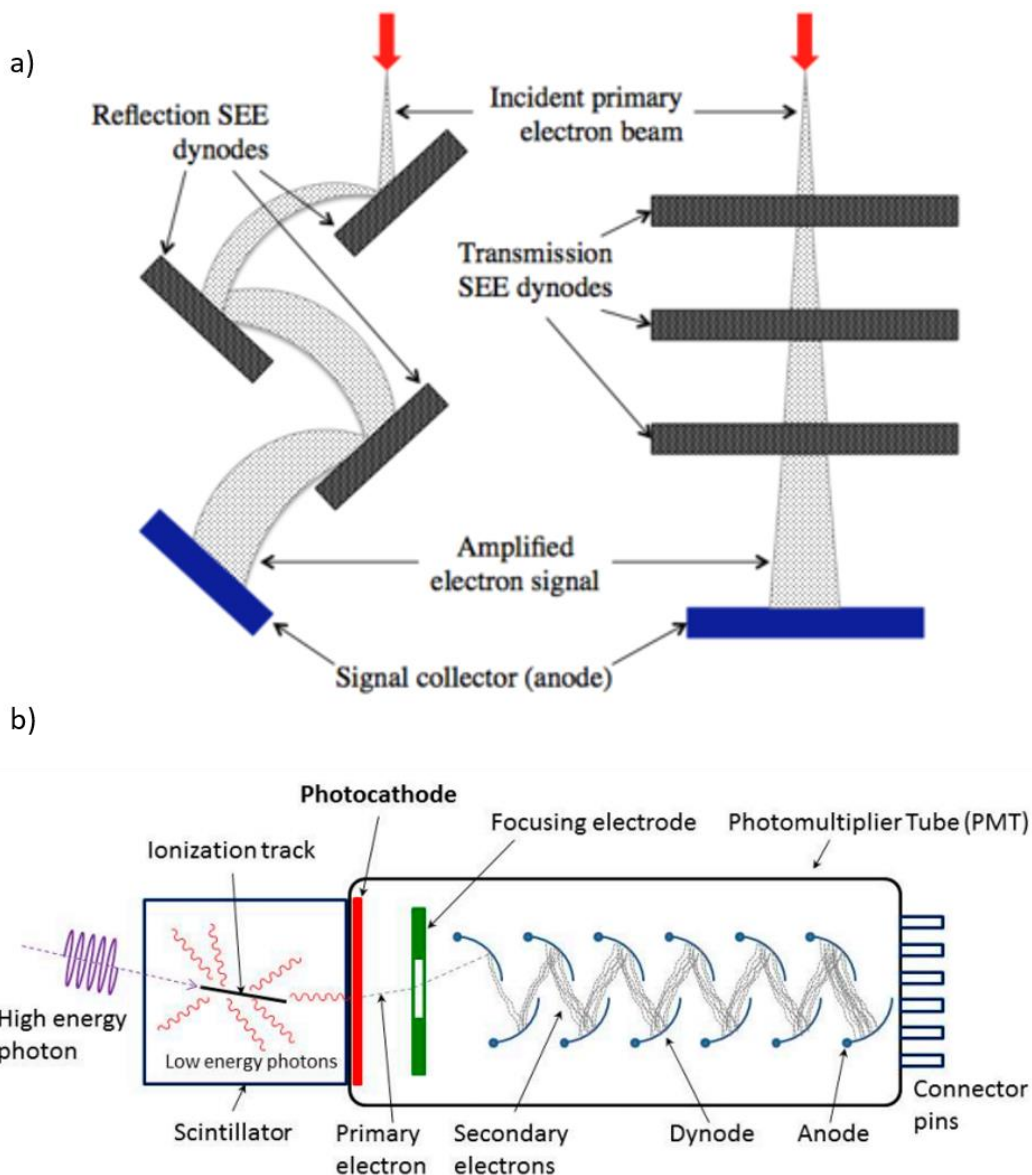


Figure 1.15. a) Reflection (left) and transmission (right) dynode structures demonstrating different electron propagation mechanisms. b) A photomultiplier tube schematic encompassing a reflection photocathode mode. Images reproduced from reference 48.

The fundamental difference between the two dynode structures are the thicknesses. Reflective dynodes can be in the order of micro-meters or larger. For transmissive dynodes, primary electrons

must penetrate deep enough into the material to allow secondary electrons to escape out the other side with enough energy which requires the material to be very thin. However, transmissive dynodes films must be mechanically stable for its applications, so a bias, or internal drift field, is often applied across the material to pull the electrons through.

Commercially, reflection secondary electron emission is the more commonly used technique in industry with transmission secondary emission still being developed in laboratories. Reflective dynodes gave short dynode lifetimes towards the last few gain stages in a PMT due to the higher, more damaging currents. Transmissive dynodes however experience lower average currents as highly energetic electrons lose kinetic energy when traversing through the dynode. This means that less damage is incurred on the components of a transmissive dynode device which results in a better overall lifetime. Other advantages of the transmissive arrangement include: (1) a reduction in signal transit time and dead time, (2) a reduction in detected signal fluctuations, (3) uniform response over the area of the dynode due to angles of dynodes in the device, and (4) a reduction in charge build-up effect due to the thin nature of transmissive dynodes.<sup>51</sup>

The SEY of dynodes can be improved by the use of a negative electron affinity (NEA) layer. This is usually done by coating the surface with a monolayer of atoms, or adsorbates, or by surface reconstruction.<sup>52</sup> NEA occurs when the vacuum level is lower than the conduction band of the material making the emission of electrons at the vacuum interface favourable (Figure 1.17).<sup>47</sup>

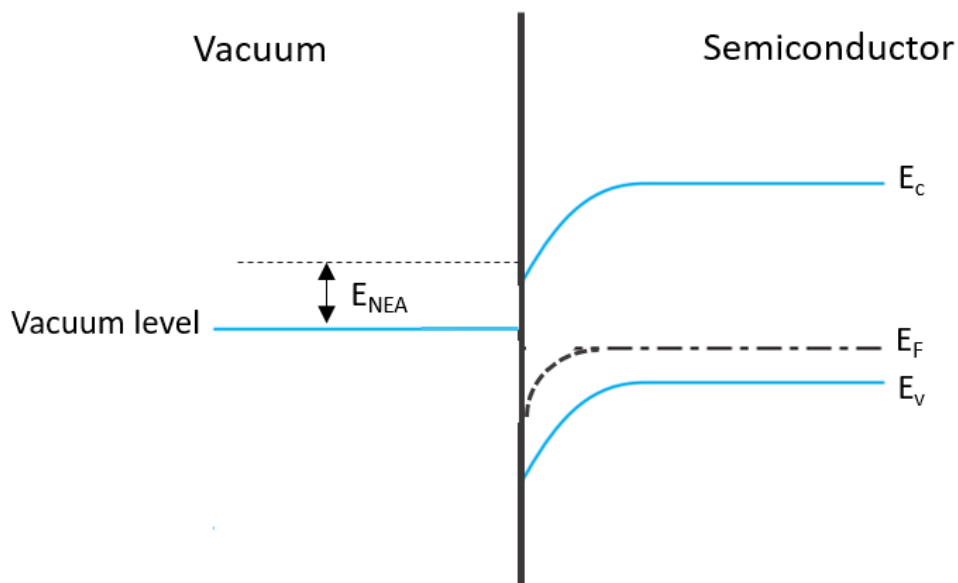


Figure 1.17. conduction band bend at surface, NEA is difference between conduction band minimum and the vacuum level. Samples without enhancement would show vacuum level higher than conduction band minimum.

The extent of NEA is modified by appropriate surface terminations e.g. Cs and Cs-O on semiconductors,<sup>53</sup> or H-termination on diamond.<sup>54</sup> Cs is also effective at replenishing lost electrons however, it is very reactive in air and is often replaced by Li-O for certain systems. For hydrogen terminated p-type diamond, the conduction band lies  $\sim 1.1$  eV below the vacuum level because of the

surface dipole created.<sup>55</sup> The  $\delta^+$  H draws electrons from the more electronegative carbon lattice resulting in their feasible escape into the vacuum.

In addition, NEA layers are sensitive to high energy electron radiation, the process by which NEA layers are stripped away is called electron stimulated desorption (ESD). Consequently, the use of NEA in transmissive dynodes results in longer lifetimes than the corresponding reflective arrangement as emitted electrons are lower in energy.

Dynode materials aim to preserve as much primary electron energy as possible whilst avoiding electron scattering. Research into reflective dynodes began in 1930s where wide band-gap insulators – for example, alkali halides – were used as they showed good SEY. However, non-conducting materials cannot sustain secondary emission for significant periods of time due to the build-up of positive charge. More recently, atomic layer deposition (ALD) has shown potential in synthesising ultra-thin films, in the order of 10 nm, as this would decrease the region of depleted electrons. Such materials included alkali-oxides such as  $\text{Al}_2\text{O}_3$  and  $\text{MgO}$ . Two projects stemmed from ALD technology: large-area picosecond photo-detector (LAPPD) for the development of MCPs,<sup>56</sup> and MEMBrane, using micro-electro-mechanical systems (MEMS) for fabricating ultra-thin transmission dynode materials.<sup>57</sup>

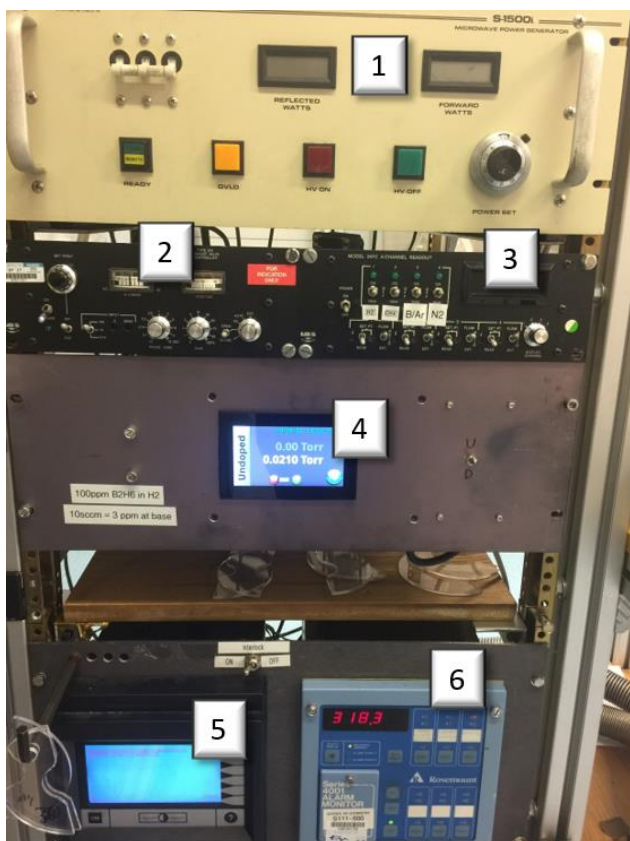
Research into transmission dynodes began 30 years after the discovery of reflective dynodes. In the 1970s, semiconducting materials such as GaAs and Si, with a NEA terminating layer such as Cs or Cs-O were studied for their application as transmissive dynodes in image tubes.<sup>48</sup> Semiconductors have a large escape depth and excellent electron transport properties and therefore, exhibit little electron scattering.

The discovery of H-terminated diamond as an NEA material in the 1990s triggered their use as electron emitters in photocathodes, and secondary electron emitters in dynodes for electron multiplication devices. This is because H-termination is a relatively simple surface treatment. Most research conducted since the discovery has been for reflection SEE properties due to the difficulty in fabricating ultra-thin films however, recent advances in the MEMBrane project have made the prospect of this tough fabrication more feasible.

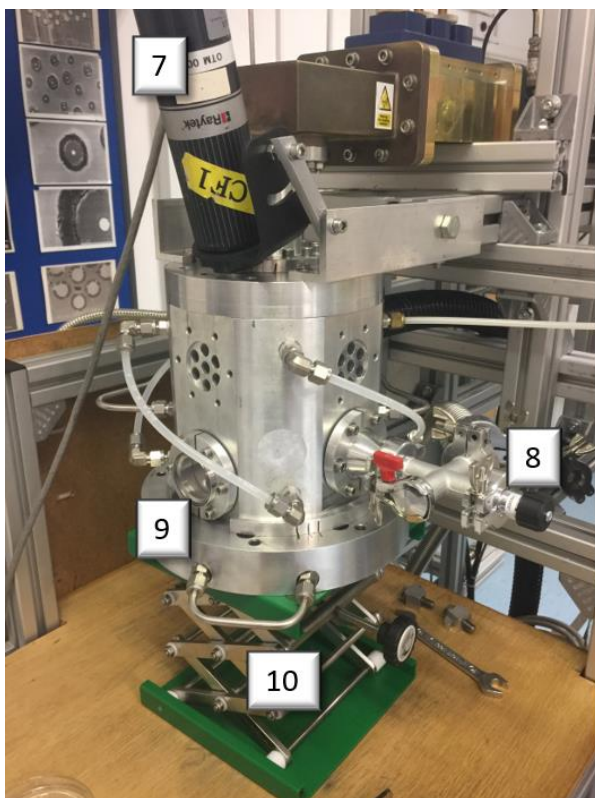
## 2 Experimental Methods

### 2.1 The MW PECVD Reactor

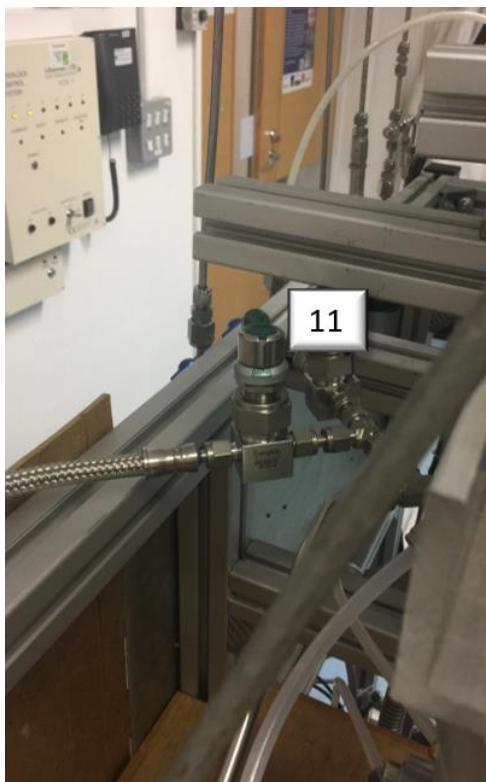
A 1.5 kW MW plasma-enhanced CVD reactor has been used to grow the diamond samples for this work. The reactor is labelled below.



1. Microwave Power Supply –  
Striking power at 45%, then set to 1.5 kW
2. Butterfly Valve controller and Exhaust controller for “gases out”, and pressure dial  
Pressure dial raised with MW power to 150 Torr
3. Mass flow controller (MFC) for “gases in”  
Set to correct flow rates
4. Pressure display  
Should be at base pressure before striking
5. Pyrometer (temperature display)  
Emissivity set to 0.19
6. Interlock System Control  
Shuts Solenoid valve if tripped

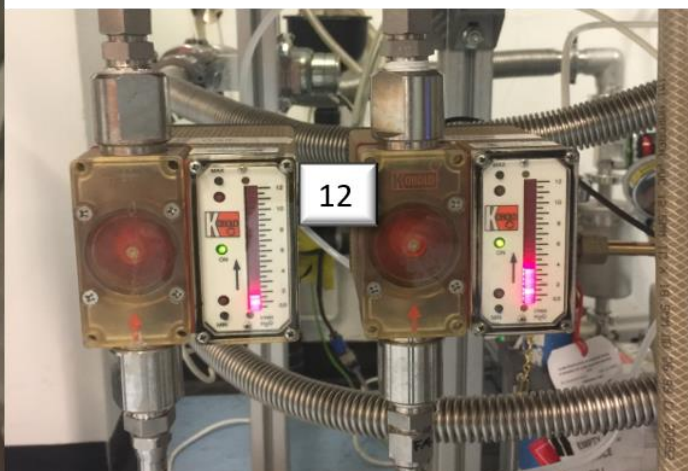


7. Pyrometer  
Check that cross hairs point to the centre of the sample
8. Leak Valve  
Check that it is closed before pumping down
9. Baseplate  
O-ring must be clean and snug to avoid leaks, baseplate bolts also screwed in
10. Lab jack  
Used to gently raise and line-up baseplate



11. Gas-line tap  
Must either be closed or have Ar flowing

12. Water flow meters  
Cools outside of reaction chamber



## 2.2 Sample Fabrication

A total of 14 p-type diamond samples were grown in the MW PECVD reactor: 8 of the samples were heavily boron-doped diamond (BDD) grown for varying times, and 6 of the samples were residual boron-doped diamond (RBDD) each grown for 1 h. The table below shows each labelled sample.

Table 2.1. Summary of the samples produced in this study.

Sample	Substrate	Material	Height / $\mu\text{m}$	Growth time / h	Cuts / mm
BDD1	p-type Si	heavy BDD	0.71	1	5x10
BDD2	p-type Si	heavy BDD	1.29	2	5x5, 5x5, 5x10
BDD3	p-type Si	heavy BDD	1.99	3	5x5, 5x5, 5x10
BDD4	p-type Si	heavy BDD	2.7	4	5x5, 5x5, 5x10
BDD5	p-type Si	heavy BDD	3.17	5	5x5, 5x5, 5x10
BDD10	p-type Si	heavy BDD	7.13	10	2x10, 8x10
BDD15	p-type Si	heavy BDD	27.77	15	4x10, 6x10
BDD2 for RBDD	p-type Si	heavy BDD		2	10x10
RBDD1	p-type Si	residual BDD		1	10x10
RBDD2	p-type Si	residual BDD		1	10x10
RBDD3	p-type Si	residual BDD		1	10x10
RBDD4	p-type Si	residual BDD		1	10x10
RBDD5	p-type Si	residual BDD		1	10x10
RBDD6	p-type Si	residual BDD		1	10x10

### 2.2.1 BDD

Seven p-type Si substrates ( $10\text{ mm}^2$ , 0.5 mm thick) were cleaned by sonicating them one after another in methanol, acetone, ethanol and deionised water for 5 min each. They were then left in carboxyethylsilanetriol disodium salt 25wt% for 10 min to add a sticky coating to the substrate before thoroughly rinsing in deionised water and leaving in diamond nanoparticle solution (4-8 nm particle size) for a further 10 min to seed the substrates as shown in Figure 2.1a. The diamond nanoparticles adsorb into crevasses in the Si substrate surface which helps initiate the growth, by providing growth propagation sites, and ensures that the film growth is uniform. The seeded substrates were stored at RTP until used for diamond growth.

The samples were grown for 1, 2, 3, 4, 5, 10 and 15 hours. Prior to each growth, the substrate was loaded onto a substrate holder sitting on top of a 0.15 mm diameter molybdenum wire. The substrate was then left to pump down overnight in the sealed reaction chamber to evacuate any air and other contaminants that can interfere with the growth. Pumping down is especially important when growing with boron as the borane gas used is very sensitive to air. The growth was done the next day under these set of conditions:

- Flow rates (sccm):  $\text{H}_2$ : 288;  $\text{CH}_4$ : 12.6; 100 ppm  $\text{B}_2\text{H}_6$  in  $\text{H}_2$ : 12.6

- Emissivity (EMS): 0.19
- MW power: 1.5 kW
- Pressure: 150 Torr
- Temperature range: 870 – 950°C

The specific growth conditions were chosen to be as standard as possible. The thermal contact that the Mo wire makes with the substrate holder ensures that the temperature range of the sample is between 860 – 980°C. This temperature range gives a good balance between film quality and growth rate. Higher temperatures would lead to more clusters of sp<sup>2</sup> graphite whereas lower temperatures slow the growth rate considerably. The emissivity is necessary for measuring the temperature of the sample through a vacuum and must be calibrated for a specific material, the calibration for diamond gave a value of 0.19. The combination of 1.5 kW and 150 Torr gives a mid-range power density in the reactor. In terms of the flow rates, the total flow rate equates to 313.2 sccm which is comprised of 4% methane in hydrogen, and a small amount of diborane (0.0001 sccm) as the diborane flow is almost entirely H<sub>2</sub>. The total flow rate of gas makes little difference to the growth, so long as the residence time of the gas in the chamber is not large enough for the gas to go stale.

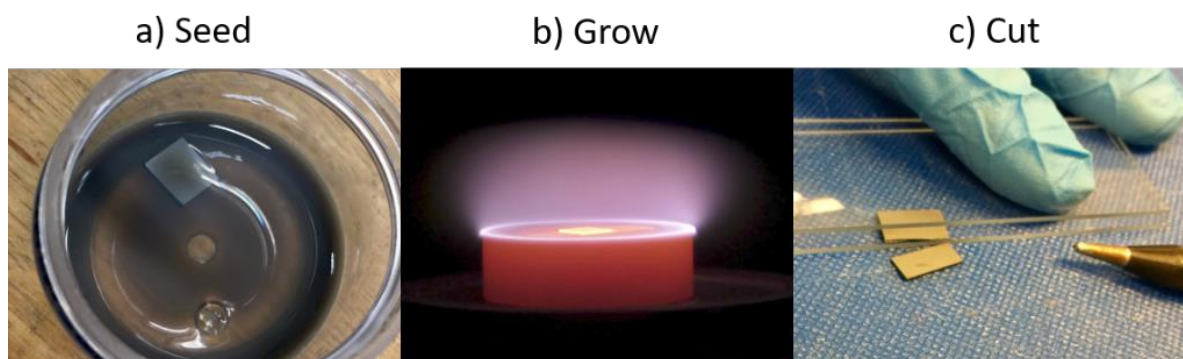


Figure 2.1. CVD diamond growth process including: a) seeding the p-type Si substrate in a diamond nanoparticle suspension; b) growing the seeded substrate in the ASTeX MW plasma reactor; and c) cutting the diamond sample in half using a diamond scribe for SEM analysis.

For the 10 and 15 h samples, the growths were split up into multiple days. They were left under vacuum during the night and the growth was re-initiated the following day.

After the growth, the methane and borane gas taps were switched off and the film was left in the presence of a H<sub>2</sub> plasma for a further 2 min to hydrogen terminate the film. The samples were cut in half, using a diamond scribe (Figure 2.1c), and SEM images were taken of the cross section and the surface.

### 2.2.2 RBDD

A further seven p-type Si substrates were seeded analogous to the method in 2.1.1 BDD. Firstly, one regular BDD sample was grown for 2 h in the MW reactor under the exact same conditions as the

2.1.1 *BDD* to ensure the experiment is reproducible. Six subsequent samples were then grown, each for 1 h, using the residual boron in the chamber (RBDD1 – RBDD6) under similar conditions to the first BDD growth but without the flow of diborane gas. The growth parameters are listed below:

- Flow rates (sccm): H<sub>2</sub>: 300; CH<sub>4</sub>: 12.6
- Emissivity (EMS): 0.19
- MW power: 1.5 kW
- Pressure: 150 Torr
- Temperature range: 870 – 950°C
- Wire: 0.15 mm Mo

The initial BDD sample was grown for 2 h and not 1 h because the growth rate of BDD is likely to be much slower in this time range, so the growth time is doubled to have a better chance of obtaining consistent film thicknesses which is important for conducting electrical measurements on the samples.

The substrate for BDD was pumped down in the reaction chamber overnight prior to growth to avoid reactions between the diborane-containing gas phase and air, whereas the RBDD substrates were only pumped down for 20 min prior to growth as no additional diborane is introduced. This allowed the growths to be done in quick succession.

After the growth, the methane gas tap was switched off and the sample was left in the presence of a H<sub>2</sub> plasma for a further 2 min to hydrogen terminate the film, similar to the method in 2.1.1 *BDD*.

## 2.3 Scanning Electron Microscopy

Scanning Electron Microscopy (SEM) is a surface characterisation technique that uses a focused beam of electrons to scan the topography of a material. The electron beam excites the atoms on the surface producing secondary electrons which are measured in relation to the incident beam to give an image with resolution better than 1 nanometre.<sup>58</sup>

A JEOL JSM-IT300 Scanning Electron Microscope was used to image the cross section and top surface of each of the seven BDD samples grown. The instrument uses a hot tungsten filament to produce the electron beam *via* thermionic emission.

## 2.4 Raman Spectroscopy

Raman spectroscopy is a non-destructive, qualitative technique for identifying the molecular content of a sample. It identifies the molecular species present in a sample by measuring vibrational, rotational, and other low frequency modes.<sup>59</sup> Monochromatic light (of frequency close to the infrared – UV vis region) interacts with molecular vibrations and lattice phonons to give off light corresponding to the quantised vibrational states (that obey the selection rules) of the species

present. The Raman emission line intensity is proportional to the quantity of a certain species in the sample therefore, comparisons can be made between different peak heights in a spectrum to give their relative proportions.

Pure polycrystalline diamond exhibits a strong, narrow peak at  $1332\text{ cm}^{-1}$  (FWHM =  $\sim 2\text{ cm}^{-1}$ ) corresponding to the  $sp^3$  C-C bond vibration.<sup>60</sup> Graphite-related peaks are usually observed in CVD diamond samples as an impurity and is typically localised in grain boundaries. Graphite can split into two bands: The G-band ( $1583\text{ cm}^{-1}$ ) which corresponds to the  $sp^2$  C-C stretching mode; and the D-band ( $1350\text{ cm}^{-1}$ ) which is a defect-induced mode resulting from disordered  $sp^2$  carbon.<sup>61</sup> The G-band can scatter forwards if the graphite is nanocrystalline, or backwards if it is amorphous.<sup>62</sup> The broad signal at  $\sim 970\text{ cm}^{-1}$  is assigned to silicon.

This study uses a Renishaw 2000 Raman instrument with a laser excitation wavelength of 514 nm (green) scanned over the range  $600 - 2000\text{ cm}^{-1}$ .

## 2.5 Van der Pauw Setup

The van der Pauw (VDP) method is a technique used to measure the resistivity of a two-dimensional material of arbitrary shape.<sup>63</sup> For reliable measurements, samples must have a constant thickness and uniform resistivity throughout. Four contacts are made around the perimeter of the sample and a voltage is applied in all the possible directions to yield a current that is measured and averaged across the different directions.

The van der Pauw (VPD) method was used to obtain sheet resistances which will then be used to calculate the resistivity once the SIMS depth analysis returns as  $\rho = R_s \times h$ , where  $h$  is the BDD height (m),  $R_s$  is the sheet resistance ( $\Omega$ ) and  $\rho$  is the resistivity ( $\Omega\text{m}$ ).

## 2.6 Secondary Ion Mass Spectrometry

Secondary Ion Mass Spectrometry (SIMS) is a destructive technique is to measure the surface composition of a solid surface. The solid surface is bombarded with a highly energetic primary ion beam leading to the ejection of secondary ions in a process known as sputtering. The mass/charge ratio of the secondary ions are measured in a mass spectrometer to determine the elemental and isotopic composition of the solid surface.

SIMS is a quantitative and qualitative technique as it measures both the composition and the relative concentrations to detection limits ranging from parts per million to parts per billion. Over time, the primary ion beam (usually  $\text{Ar}^+$  or  $\text{Ga}^+$ )<sup>64</sup> penetrates deeper into the material therefore, a depth profile of concentration as a function of sample height can be obtained with the use of SIMS.

### 3 Results and Discussion

#### 3.1 BDD Growth Calibration

The growth rate of BDD is dependent on the type of reactor and the growth conditions used. As discussed earlier, there are 3 main types of CVD reactors: hot filament, plasma, and combustion flame. Each type has many sub-types of varying geometries and materials which influences the growth rate. At present, there is an increasing demand for high quality diamond films of specific thickness, conductivity and morphology, and there is a lack of characterisation for the different reactors in the CVD diamond growth industry. Therefore, the aim of this experiment is to begin to characterise the ASTeX microwave plasma enhanced CVD (MW PECVD) reactor used in the Bristol diamond laboratory by conducting a growth calibration experiment.

##### 3.1.1 SEM Images

SEM images were taken of each sample. The sample heights and grain sizes were measured on *ImageJ* and plotted against the growth time. Raman spectra were also taken for some of the samples to examine the quality.

Images were taken of the cross section and top surface of each of the seven samples grown. The cross sections displayed below (Figure 3.1 and Figure 3.2) are of the heavily boron doped diamond films grown for 1, 2, 3, 4, 5, 10 and 15 h (BDD1 – BDD5, BDD10 and BDD15)

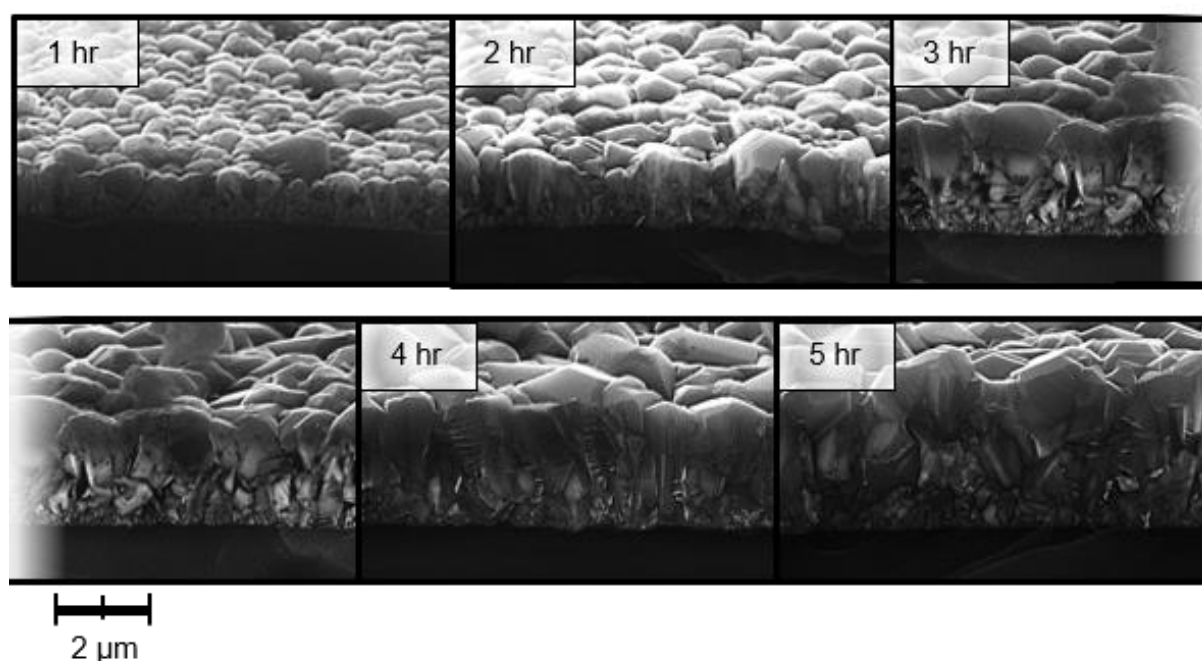


Figure 3.1. Cross sectional SEM images of BDD1, BDD2, BDD3, BDD4 and BDD5, with the growth time labelled on each image. The BDD3 image is split into two halves on each to allow visual comparisons. The scale bar at the bottom left applies to all images (magnification =  $\times 10000$ ).

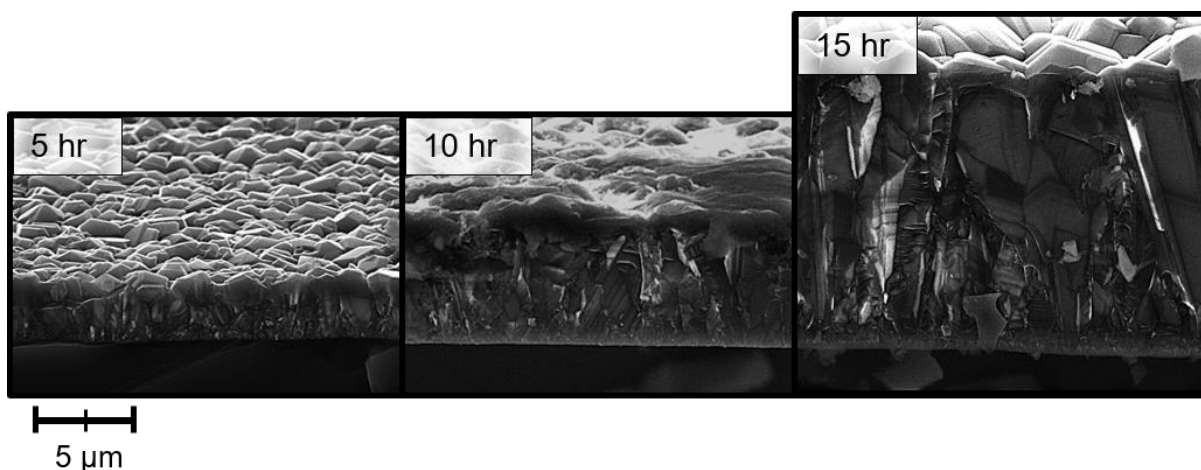


Figure 3.2. Cross sectional SEM images of BDD5, BDD10 and BDD15, with the growth time labelled on each image. The magnification is reduced to  $\times 5000$ .

The cross sectional face of each image was mounted at an angle of  $30^\circ$  to the camera lens so the polycrystalline surface can also be seen. conductive tape was applied to the sample mount to avoid charging of the sample.

### 3.1.2 Raman

BDD2, BDD5, BDD10 and BDD15 were all measured using Raman spectroscopy (Figure 3.3).

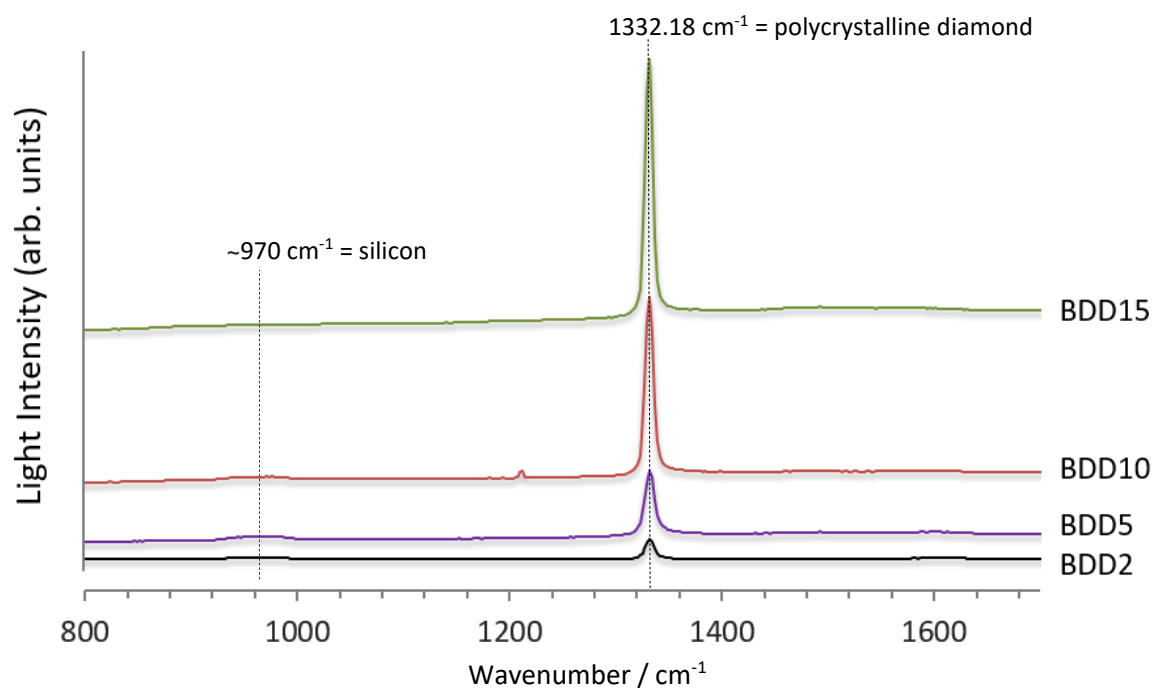


Figure 3.3. Raman spectra of heavily doped samples BDD2, BDD5, BDD10 and BDD15 in the range  $800 - 1700 \text{ cm}^{-1}$ . The spectra are position in order of growth time hence the light intensity units are arbitrary.

Both the increase in the diamond peak intensity and the decrease in the silicon signal intensity are consistent with an increasing film thickness with growth time which has also been observed in the literature.<sup>60</sup>

The quality of the films in Figure 3.3 are all good as no graphite-related peaks are observed in any of the spectra. Furthermore, the FWHM of the diamond peaks decreases with increasing film thickness from  $10.41 \text{ cm}^{-1}$  (BDD2) to  $8.24 \text{ cm}^{-1}$  (BDD15). The order of these values is consistent with values found in recent literature, which is substantially higher than the FWHM of pure polycrystalline ( $\sim 2 \text{ cm}^{-1}$ ). The FWHM is sensitive to the growth conditions and peak broadening is attributed to impurities and defects in the sample largely caused by nitrogen.<sup>49</sup>

### 3.1.3 Growth Rate Analysis

The thickness of each film was analysed using *ImageJ*. After calibrating the scale bar shown at the bottom of each SEM image, the image was rotated by a few degrees to straighten the Si – BDD interface. Several vertical lines (10-12) were then drawn and measured at random positions along the cross section from the Si – BDD interface to the crystal surface. The average line height was then divided by  $\sin(70^\circ)$  as the SEM sample mount is angled at  $30^\circ$  from the normal. Figure 3.4 shows the analysis done for one SEM image of sample BDD 5 (BDD grown for 5 hours). The table underneath shows the measured heights of the lines.

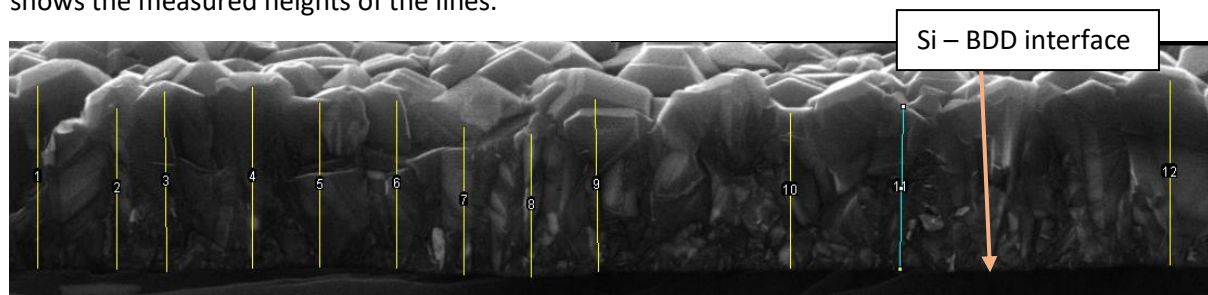


Figure 3.4. Cross sectional SEM image of BDD5 (top) with 12 lines drawn for height analysis, and a table of each line height in nanometres (bottom).

Table 3.1. Line heights (nm) measured in ImageJ for BDD5 (Figure 3.4).

Line	Height / nm	Line	Height / nm
1	3239.896	7	2619.916
2	2859.908	8	2539.919
3	3200.148	9	3060.49
4	3219.897	10	2759.912
5	2919.907	11	2900.528
6	2979.905	12	3279.895

This process was repeated for 3 different areas of the cross section on each heavily-doped sample and averaged to give an accurate film thickness. The thickness of each sample was then plotted against the growth time to establish the growth rate of BDD in the ASTeX MW reactor under the specific set of conditions used (Figure 3.5).

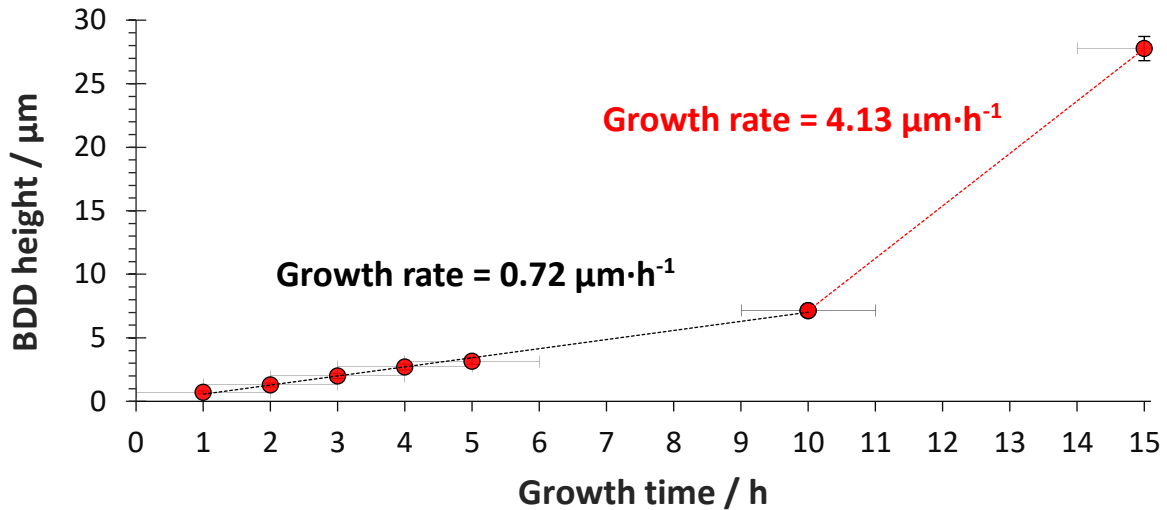


Figure 3.5. Growth calibration curve showing the cross sectional heavily boron doped diamond height against the growth time with error bars of the standard error plotted.

In this experiment, BDD samples were initially grown for 1, 2, 3, 4 and 5 h. It was found that BDD5 grew to a surprisingly low height (3.17 µm) – therefore, a further two samples were grown for 10 h and 15 h in order to explore the growth rate around a more appropriate thickness where BDD is used for some of its applications, e.g. transmissive dynodes. Here, BDD must be mechanically stable upon removal of the Si substrate which means growing to a thickness of at least 10 µm, which was achieved by the latter two growths.

The initial growth rate was 0.72 µm·h<sup>-1</sup> and continued linearly for 10 h before rising to 4.13 µm·h<sup>-1</sup> between BDD10 and BDD15. This suggests that there is a change in the deposition mechanism during this time which results in a faster deposition rate. This change occurs between 10 and 15 h of growth which means the growth rate at 15 h is at least 4.13 µm·h<sup>-1</sup>. Ideally, more data points during this growth time would show more precisely where the change occurs – however, growths of these lengths take multiple days. It is inferred from the SEM images (Figure 3.2) that the change in growth rate occurs closer to 10 h than 15 h of growth as the observed change in crystallite alignment occurs at this point.

Figure 3.6 shows a cross-section SEM image of BDD15. The red line parallel to the Si – BDD interface shows the height of BDD10 (7.13 µm) corrected for the angle of the SEM mount. Below the red line there is an abundance of grain boundaries which is known to inhibit growth, whereas above the red line, there is a notable change in the orientation of the crystal growth – crystals have grown vertically which is demonstrated by the vertical grain boundaries and more ordered, continuous crystal structures. It is likely that this change in crystal structure is responsible for the faster growth rate of 4.13 µm·h<sup>-1</sup> as the crystallites above the red line are bigger thus there are fewer grain boundaries and more surface for the carbon to deposit on.

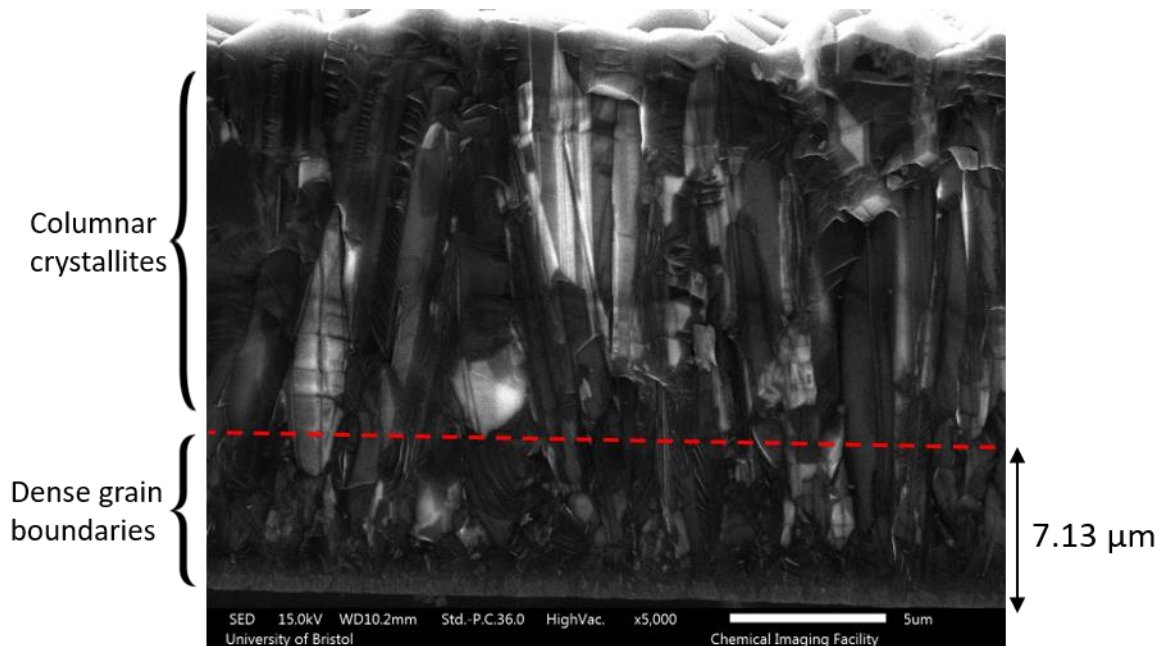


Figure 3.6. Cross sectional SEM image of BDD15. The red line shows the height of BDD10 (7.13  $\mu\text{m}$ ) adjusted for the angle of the sample mount.

The growth of BDD on a silicon substrate can in fact be split into 3 regimes of growth: homoepitaxial wetting; growth competition phase; and fast columnar growth.

Homoepitaxial wetting (Figure 3.7a) refers to the lateral growth of BDD from the adsorbed diamond nanoparticle seeds. During the pre-treatment of the substrate, diamond nanoparticles adsorb into the crevasses of the silicon providing growth initiation sites as diamond prefers to grow on diamond rather than silicon. The growth proceeds laterally until the surface of the substrate is fully covered. This stage of growth typically lasts under 1 h and grows to a few nanometres thick.

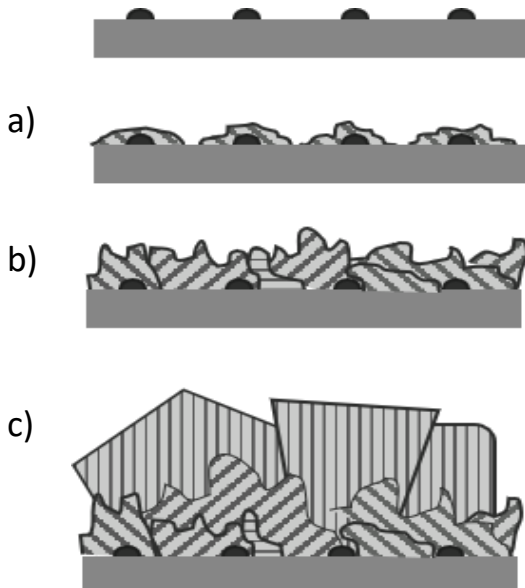


Figure 3.7. Concept diagram of the different stages of growth: a) homoepitaxial wetting; b) growth competition phase; and c) fast columnar growth

The next stage is the growth competition phase (Figure 3.7b) which is characterised by a dense layer of grain boundaries. In this regime, individual crystallites grow in random directions and obstruct the growth of other crystals. Some crystallites prevail and grow into the available space, while other crystallites collide and stop growing. This results in a layer of dense grain boundaries and small crystals ( $< 1 \mu\text{m}$  diameter) shown by the region under the red line in Figure 3.6 (BDD15). This stage of growth typically lasts  $\sim 10$  h and grows to  $\sim 7 \mu\text{m}$  thick under the conditions used in this experiment.

The final stage is fast columnar growth (Figure 3.7c) and is characterised by large, vertical crystal columns as shown above the red line in Figure 3.6. The transition from the growth competition phase to fast columnar growth is where the change in growth rate going from  $0.72 \mu\text{m}\cdot\text{h}^{-1}$  to  $4.13 \mu\text{m}\cdot\text{h}^{-1}$  is observed for this experiment. This is because

the crystallites are more aligned and able to grow much larger providing more surface for carbon to deposit on. The polycrystalline film is thought to approach single crystal growth as there are far less grain boundaries. It is possible that the diamond has less impurities in this regime as impurities tend to reside mainly in the grain boundaries.

When comparing the growth rate of BDD with other diamond growths conducted in the Bristol diamond group using the same reactor, it becomes evident that the growth rate is very sensitive to small changes in the growth conditions. In recent experiments carried out by the diamond group, two BDD samples were grown, each for 3 h under the same conditions used in this study, but with half the flow rate of diborane (0.00005 sccm). They reported growth rates of  $0.35 \mu\text{m}\cdot\text{h}^{-1}$  and  $2.37 \mu\text{m}\cdot\text{h}^{-1}$  for samples grown at  $800^\circ\text{C}$  and  $1015^\circ\text{C}$  respectively (unpublished) which demonstrates the considerable influence temperature has on the growth rate. During a growth, the temperature can fluctuate  $\pm 20^\circ\text{C}$  which implies fluctuations in the growth rate hence, it is very difficult to reproduce a BDD sample under a constant set of conditions.

### 3.1.4 Grain Size Analysis

The grain size also changes with growth time. The grain sizes of BDD3, BDD5, BDD10 and BDD15 were measured using SEM images of the crystal surfaces in *ImageJ*. Three quadrants were randomly selected for each sample to ensure the same area was measured. Figure 3.8 shows an example of one quadrant on one BDD5 SEM image. Only the grains that were fully in the quadrant were outlined and measured. This process was repeated 3 times for each sample.

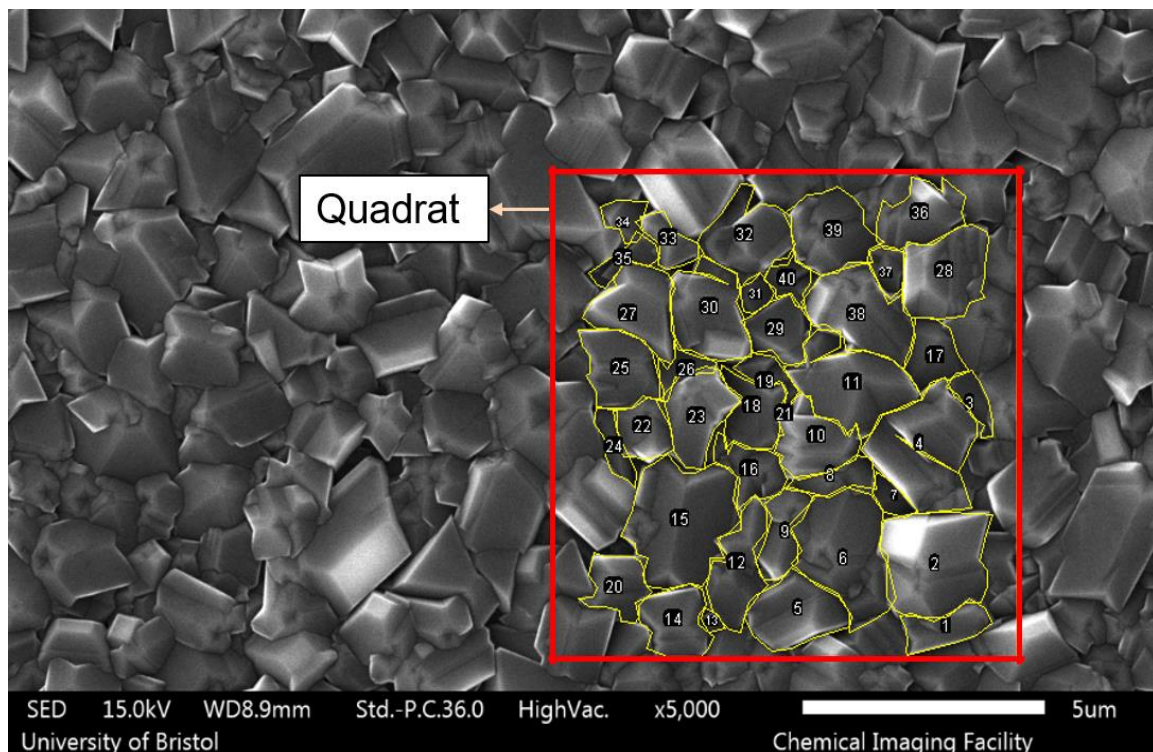


Figure 3.8. Crystal surface SEM image of BDD5. The quadrat outlines the region where grain sizes are measured which was done thrice for each sample.

Approximately 60 – 70 grain areas were obtained for each sample. The diameters were then plotted on histograms in MATLAB and they were fitted using a Rician distribution (Figure 3.9, left) so that the mean and STD dev grain diameter for each sample was plotted against the sample thickness (Figure 3.9, right).

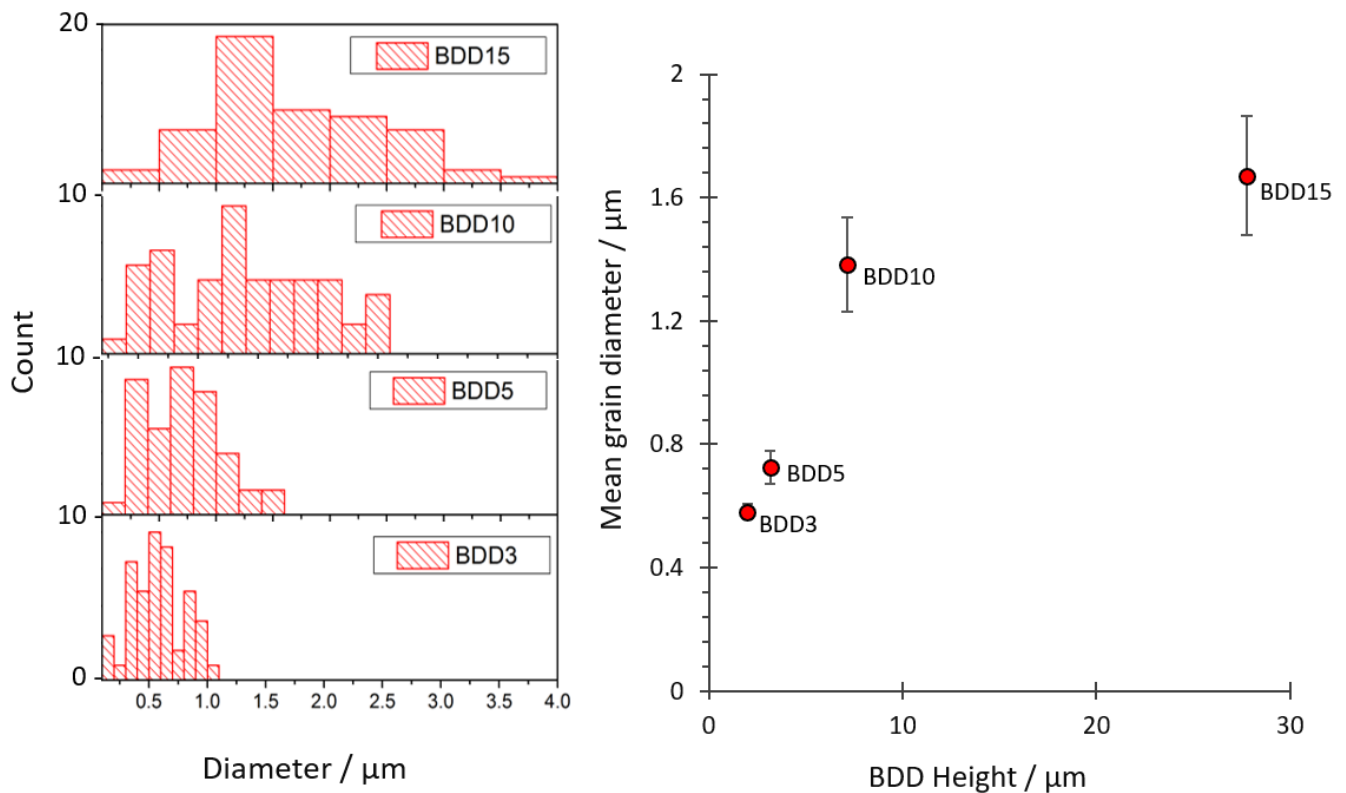


Figure 3.9. Stacked histograms of BDD3, BDD5, BDD10 and BDD15 (left) displaying the grain count against the grain area's diameter of each grain measured fitted using the Rician function on MATLAB. And a graph (right) of the average grain diameter against the sample's cross sectional height.

According to Figure 3.9 (right), the mean grain size increases linearly with the film thickness from BDD3 to BDD10, then begins to plateau after BDD10 i.e. when the film thickness is 7.13 μm. The rate of increase of grain size with respect to the film height falls from 0.16 before BDD10 to 0.013 after BDD10, a factor of 10 difference. This complies with the observed change in growth rate after BDD10 (Figure 3.5) as the crystals are more aligned in the fast columnar growth regime therefore, lateral changes in the crystal size are heavily restricted.

The Standard deviation is also shown to increase with the mean grain diameter. Even at large average crystal sizes, small crystals (< 0.5 μm diameter) are still present which means the polydispersity of grain sizes increases for larger mean grain diameters.

## 3.2 RBDD Experiment

Another important feature of the MW reactor when growing diamond is the amount of boron contamination in the reaction chamber. Boron can absorb deep into hot metallic materials; boron mainly seeps into the pumping ducts and the reactor walls near the substrate as these areas experience high concentrations of boron gas.<sup>59</sup> N-type, or intrinsic diamond cannot be grown in a boron contaminated chamber as the residual boron can be recycled into subsequent growths – however, it is possible to grow lightly doped p-type diamond films using the residual boron in the chamber.

The aim of this section is to investigate how the concentration of boron changes in successive samples grown in the presence of residual boron in the contaminated chamber. This type of calibration could potentially allow the accurate growth of lightly boron-doped diamond films, with known boron content, in the ASTeX MW reactor whilst saving time and cost as the reactor would not require cleaning or changing, and no additional diborane ( $B_2H_6$ ) gas is needed.

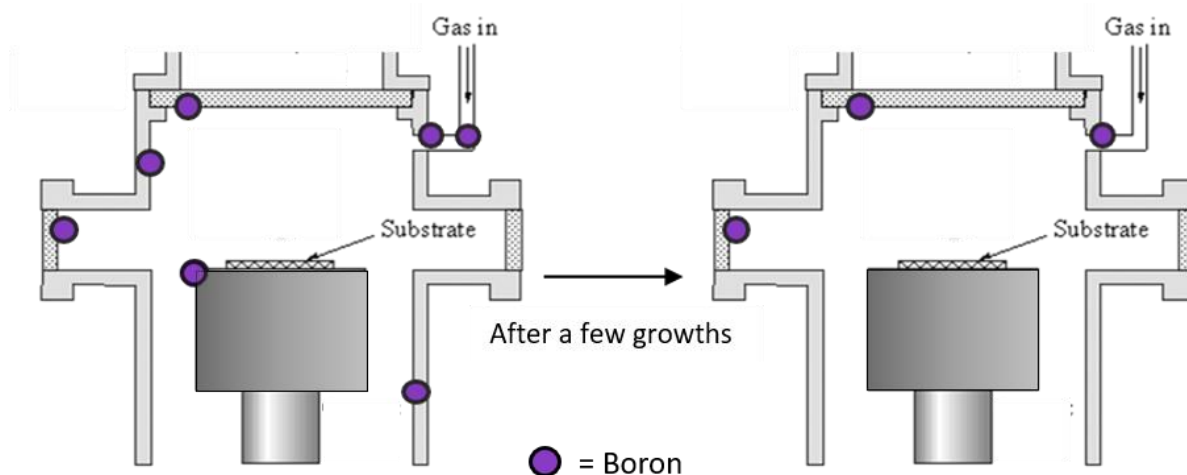


Figure 3.10. Concept diagram demonstrating the depletion of boron contamination in a reaction chamber after a few growths. The boron that is absorbed into the chamber is recycled into subsequent growths which cleans the reactor.

### 3.2.1 Raman

The Raman spectra for the residual boron-doped diamond samples all showed a rising baseline which is caused by a large fluorescent background. It is proposed that high fluorescent backgrounds could be linked to high levels of nitrogen-related defects in diamond films which, in the residual boron samples, could be due to increased air contamination (short pump down time), and/or lower B contents boron is said to compensate for nitrogen defects.<sup>65</sup> Figure 3.11 shows the rising baseline of RBDD1 and RBDD6, compared to BDD2's flat baseline. The rising baseline makes the data difficult to interpret and is thus removed in Figure 3.12 using a polynomial curve subtraction.

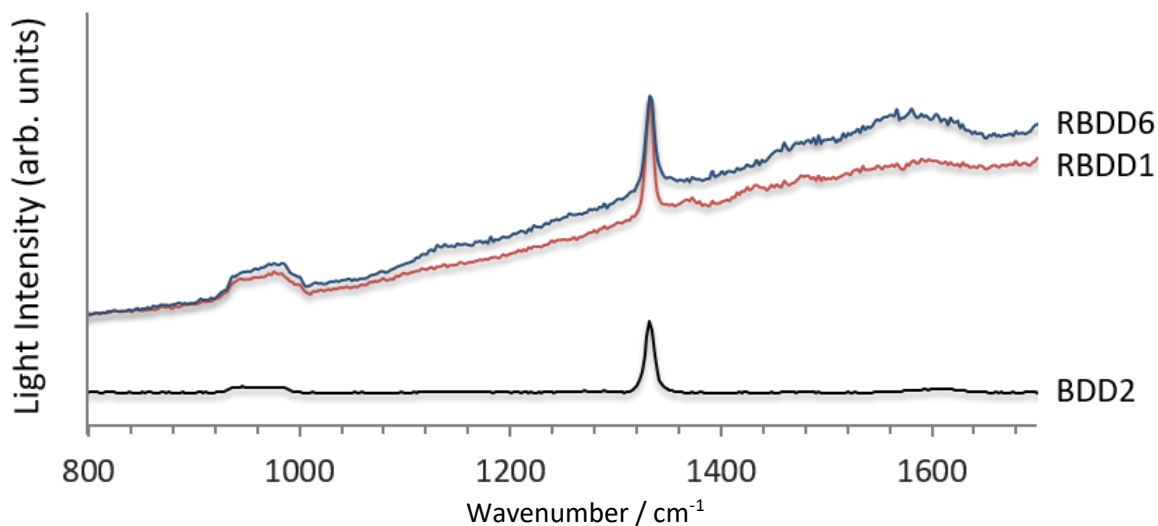


Figure 3.11. Raman spectra of BDD2, RBDD1 and RBDD6 in the range 800 – 1700  $\text{cm}^{-1}$ . All the RBDD samples display a rising baseline.

Figure 3.12 shows the Raman spectrum of BDD2 (grown for 2 h) and the ‘baselined’ spectra for RBDD1, RBDD2, RBDD3, RBDD4, RBDD5 and RBDD6 (each grown for 1 h).

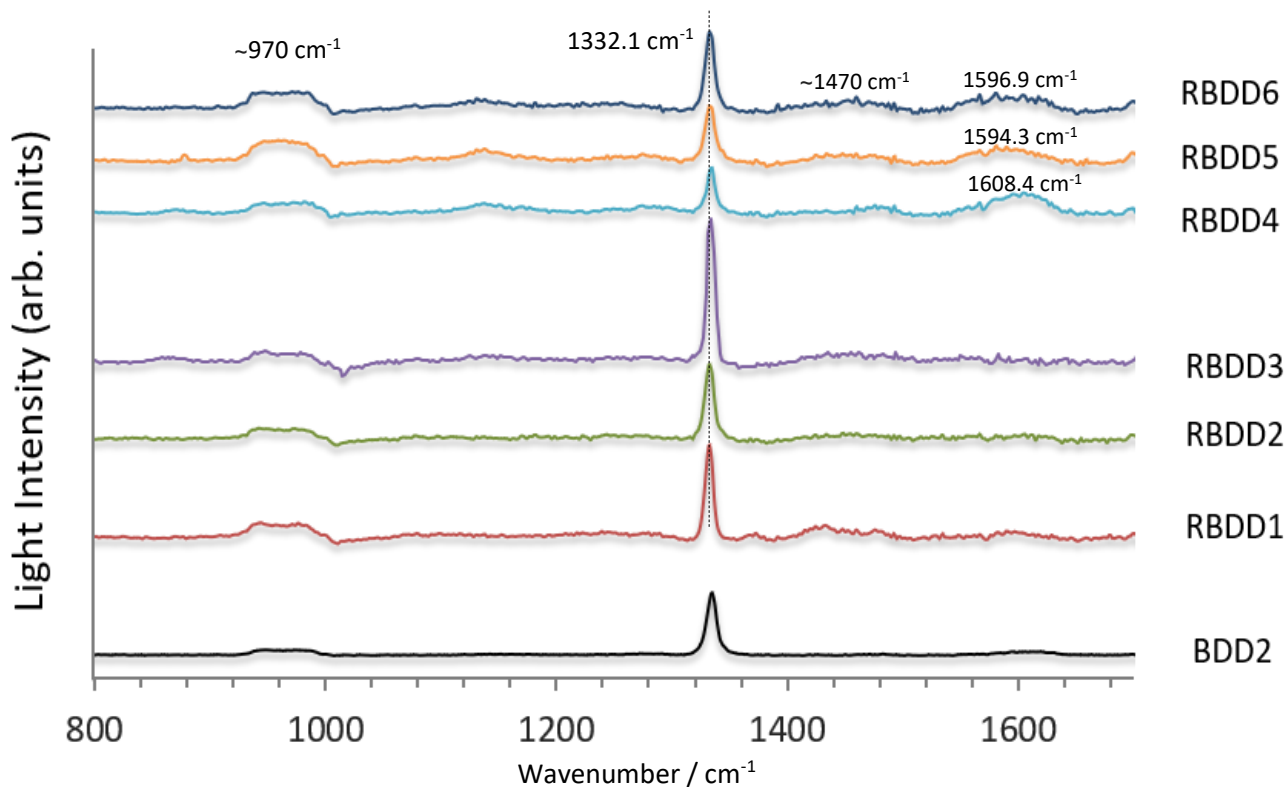


Figure 3.12. Raman spectrum of BDD2 below the baselined spectra of RBDD1 – RBDD6. All spectra shared the common diamond ( $1332.1 \text{ cm}^{-1}$ ) and silicon ( $\sim 970 \text{ cm}^{-1}$ ) peak. Later residual samples (RBDD > 3) revealed further peaks corresponding to impurities.

All the spectra above display a broad Si signal ( $\sim 970\text{ cm}^{-1}$ ) and a strong diamond peak ( $1332.1\text{ cm}^{-1}$ ) of varying intensities. It is unwise to compare the relative intensities of the diamond peaks as each film has only been grown for 1 h therefore, large errors are associated with the film thickness as the height is unlikely to be uniform across the sample in this growth regime. Graphite-related peaks are also observed in the later residual samples at  $1608\text{ cm}^{-1}$  (RBDD4),  $1594.3\text{ cm}^{-1}$  (RBDD5) and  $1596.9\text{ cm}^{-1}$  (RBDD6) which corresponds to the  $sp^2$  C-C stretching mode (G-band). These graphitic peaks are scattered toward higher positions than the literature value ( $1583\text{ cm}^{-1}$ ) which could indicate the presence of higher order, nanocrystalline graphite.<sup>62</sup>

As well as the G-band graphite peaks, there is some indication of a broad peak at  $\sim 1470\text{ cm}^{-1}$  emerging in the later samples. The literature pertaining to CVD diamond spectra are not clear about the assignment of this peak, but a general table of Raman peak assignment suggests that it could be due to C-C aromatic ring chain vibrations or asymmetric  $\text{CH}_3$ <sup>66</sup> which is not unusual given the extreme growth conditions and reactive dangling bonds.

Although the FWHMs of the RBDD diamond peaks are consistent with the values of BDD in Figure 3.3 ( $8 - 11\text{ cm}^{-1}$ ), the added spectral noise and the emergence of graphite-related peaks indicate reduced film quality in RBDD, especially in the later samples. This is likely due to increased air contamination as the reaction chamber was opened between each growth which exposes the chamber to more and more air. Nitrogen in the air incorporates well into the diamond lattice during growth creating defects and other impurities. The pump down time should be increased from 20 min to a few hours for future experiments to increase the quality of the film by removing the adsorbed N in the walls of the reactor.

Moreover, an increase in the silicon signal intensity is observed for successive RBDDs which could mean that the film height, and hence the growth rate, decreases from RBDD1 to RBDD6. This is also likely due increased air contamination as the added defects would slow down growth.

In some cases, Raman spectroscopy can be used to deduce the B content of BDD; metallic BDD has been shown to exhibit peaks at  $500$  and  $1220\text{ cm}^{-1}$ . The  $500\text{ cm}^{-1}$  shifts downfield as the B content in the film increases. However, these peaks are induced by the metallic conductivity of the sample i.e.  $[\text{B}] > 2 \times 10^{20}\text{ cm}^{-3}$ .<sup>67</sup> The samples produced in this study are semiconducting with  $[\text{B}] \approx 1 \times 10^{19}\text{ cm}^{-3}$  and thus do not exhibit such peaks on their Raman spectra.

### 3.2.2 VDP

In this experiment, BDD2 and RBDD1 – RBDD6 were all measured using the VDP setup – 1 mm length squares were graphitised at approx. 0.5 mm in from each corner of the 10x10 mm RBDD samples using a laser cutter. The graphitisation was done in an argon chamber to avoid oxidation. Contacts were then made at the centre of each graphitised square using copper electrodes connected to the instrument shown in Figure 3.13.

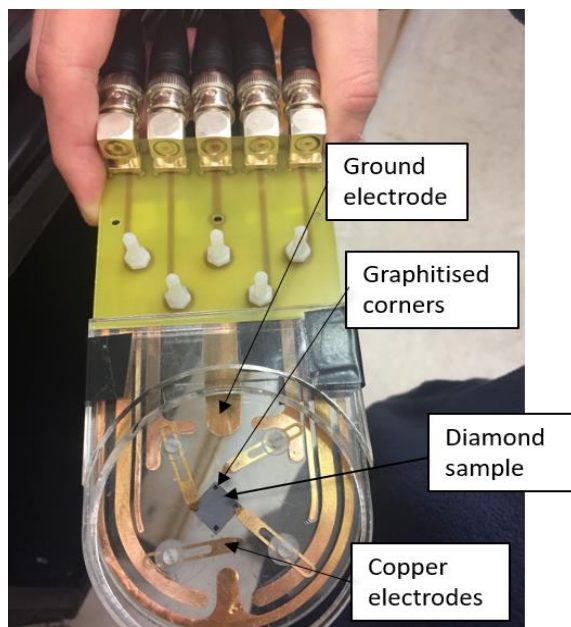


Figure 3.13. Labelled diagram of the hall effect setup used to measure the sheet resistance of a sample *via* the van der Pauw (VDP) method. The diamond sample (RBDD1) is graphitised in all four corners, with two electrodes in contact.

To generate the potential across the sample, a low current is required which can be adjusted to give the best results for a material. A current of  $1 \times 10^{-3}$  A gave the best results for heavily doped BDD2 and the first two residual doped samples (RBDD1 and RBDD2). Their measured sheet resistances ( $R_s$ ) are displayed in the table below.

Table 3.2. Sheet Resistance ( $R_s$ ) for BDD2, RBDD1 and RBDD2 with their standard errors.

Sample	$R_s / \Omega/\text{sq}$
BDD2	$0.3503 \pm 0.0008$
RBDD1	$0.3366 \pm 0.0148$
RBDD2	$0.3653 \pm 0.0184$

The remaining RBDD samples (RBDD3 – RBDD6) did not yield any results at any current tested. It is possible that these samples were too resistive, and the current could not flow through which would suggest that the conductivity is lower as the B content decreases in the later residual samples. It is also feasible that uniformity of the sample reduces in the later samples due to the increased air

contamination discussed in the 3.2.1 *Raman* section, which can obstruct the flow of current, and could also be responsible for the increased error in the measured RBDD samples.

The SIMS depth analysis will make known the film thicknesses for the RBDD samples which will be used to calculate the resistivity of BDD2, RBDD1 and RBDD2 using the equation  $\rho = R_s \times h$ . From the growth calibration curve (Figure 3.5) in section 3.1.3 *Growth Rate Analysis*, the height of BDD2 is known to be  $1.29 \pm 0.04 \mu\text{m}$  which gives a resistivity of  $4.51 \times 10^{-7} \Omega\cdot\text{m}$ . However, the thicknesses of the RBDD samples are difficult to predict – although they have each been grown for 1 h, the changing B content and/or air contamination is likely to affect the film height.

### 3.2.3 SIMS

The B content in the residually doped samples (RBDD1 – RBDD6) is expected to decrease for each successive growth until eventually, the contaminated chamber stops recycling the boron. The aim of this study is to examine the nature of the boron depletion in the reaction chamber – the depletion could be gradual, sudden, or not occur at all. This is a useful characterisation of the ASTeX MW reactor for growing lightly boron-doped diamond films which are broadly used for Schottky contacts.

SIMS is commonly used to quantify the B content in diamond films. The samples in this study have been submitted for SIMS analysis at an external facility with a SIMS instrument of high enough precision to measure the B content in lightly doped samples. Unfortunately, the results were not received before the submission deadline of this thesis.

## 4 Conclusions

The growth rate for heavily boron-doped diamond ( $[B] \approx 1 \times 10^{19} \text{ cm}^{-3}$ ) has been presented using a 1% methane in hydrogen gas phase in a MW plasma reactor. SEM imaging was used to accurately determine the film height and grain size of each sample. The growth rate was shown to increase from  $0.72 \mu\text{m}\cdot\text{h}^{-1}$  to  $4.13 \mu\text{m}\cdot\text{h}^{-1}$  after 10 hours of growth due to an abrupt change in the crystallite size. After competing for growth space, the more vertically aligned crystallites prevail as they are less likely to collide with the growth path of other crystals. The grain diameter also increased linearly with the film height at a rate of 0.16 before plateauing after 10 hours also due to the new crystallite arrangement. Other studies have shown difficulty in reproducing CVD diamond samples therefore, extra care is required when seeding the substrate and maintaining the reactor conditions to have a better control of the film thickness – however, slight variations are unavoidable and the error increases with growth time.

The depletion of boron in successive diamond growths in a contaminated chamber has not been characterised in this thesis as the SIMS data did not return in time. Nevertheless, the depletion must plateau after successive growths whether it is in the range of the measurements done in this study, or out of the range where more measurements would be required. In the case that the B content drops significantly in a reasonable range of measurements, the reactor could be used to grow lightly doped diamond films. It is also possible that the boron contamination in the reactor is so severe that the concentration of boron in residual samples does not change much.

The Raman spectra of the residually doped films demonstrated a reduction in diamond quality for the later RBDD samples. This is likely due to increased air contamination and can easily be improved by increasing the pump down time from 20 min to a few hours.

The van der Pauw data gives some indication that the early residual samples are more conductive than the later which coincides with a drop in the B content, however this is inconclusive as the absence of results in the later samples could be due to a reduction in quality.

## 5 Future work

Once the SIMS results return, the measured B content in the RBDD samples will illustrate how the dopant concentration changes with successive growths in the contaminated chamber – and whether lightly doped films can be grown in such a reactor, or whether the B content diminishes after a few growths.

Supplementary to this, Hall effect measurements can be used to quantify the carrier concentration and mobility of BDD which would enable us to see if a drop in the boron concentration corresponds to a drop in conductivity, and whether this can be used to determine the concentration of boron in a diamond film. This would require samples to be grown on insulating substrates i.e. diamond.

Other future work includes further calibration experiments to quantify how changes in the chosen growth parameters affects the growth rate of BDD, or even intrinsic diamond.

It has been proposed that the BDD samples produced in this study will be used to produce membranes which will be incorporated into dynode test structures.

## References

- 1 K. E. Spear, J. P. Dismukes and Electrochemical Society., *Synthetic diamond : emerging CVD science and technology*, Wiley, 1994.
- 2 H. M. Strong and H. M., *Am. J. Phys.*, 1989, **57**, 794–802.
- 3 W. G. Eversole and N. Y. Kenmore, *US Pat. Off.*
- 4 Ehud Arye Laniado, The History of Lab Grown Diamonds – Modern Times - Latest News, <http://www.ehudlaniado.com/home/index.php/news/entry/the-history-of-lab-grown-diamonds-modern-times>, (accessed 29 December 2017).
- 5 C. J. H. Wort and R. S. Balmer, *Mater. Today*, 2008, **11**, 22–28.
- 6 R. Abbaschian, H. Zhu and C. Clarke, *Diam. Relat. Mater.*, 2005, **14**, 1916–1919.
- 7 S. Ferro, *J. Mater. Chem.*, 2002, **12**, 2843–2855.
- 8 R. C. Burns, A. I. Chumakov, S. H. Connell, D. Dube, H. P. Godfried, J. O. Hansen, J. Härtwig, J. Hozzowska, F. Masiello, L. Mkhonza, M. Rebak, A. Rommevaux, R. Setshedi and P. Van Vaerenbergh, *J. Phys. Condens. Matter*, 2009, **21**, 364224.
- 9 M. Paul, *Diamond thin films : a 21st-century material*, 2000.
- 10 J. King, University of Bristol, 2013.
- 11 J. C. Angus, H. A. Will and W. S. Stanko, *J. Appl. Phys.*, 1968, **39**, 2915–2922.
- 12 M. Ficek, S. Drijkoningen, J. Karczewski, R. Bogdanowicz and K. Haenen, *IOP Conf. Ser. Mater. Sci. Eng.*, 2016, **104**, 12025.
- 13 E. J. Corat, N. G. Ferreira, N. F. Leite and V. J. Trava-Airoldi, *Mater. Res.*, 2002, **6**, 63–70.
- 14 M. A. Prelas, G. Popovici and L. K. Bigelow, *Handbook of industrial diamonds and diamond films*, Marcel Dekker, 1998.
- 15 J. Petherbridge, University of Bristol, 2002.
- 16 J. Bühler and Y. Prior, *J. Cryst. Growth*, 2000, **209**, 779–788.
- 17 Paritosh, D. J. Srolovitz, C. C. Battaile, X. Li and J. E. Butler, *Acta Mater.*, 1999, **47**, 2269–2281.
- 18 J. E. Butler and I. Oleynik, *Philos. Trans. A. Math. Phys. Eng. Sci.*, 2008, **366**, 295–311; discussion 311.
- 19 J. Narayan, A. R. Srivatsa and K. V. Ravi, *Appl. Phys. Lett.*, 1989, **54**, 1659–1661.
- 20 M. Werner and R. Locher, *Reports Prog. Phys.*, 1998, **61**, 1665–1710.
- 21 B. Dischler and C. Wild, *Low-pressure synthetic diamond : manufacturing and applications*, Springer, 1998.
- 22 I. Armenise, M. Capitelli and C. Gorse, *J. Thermophys. Heat Transf.*, 1996, **10**, 397–405.
- 23 S. M. Leeds, University of Bristol, 1999.
- 24 A. Cheesman, J. N. Harvey and M. N. R. Ashfold, *Phys. Chem. Chem. Phys.*, 2005, **7**, 1121.
- 25 R. G. Farrer, *Solid State Commun.*, 1969, **7**, 685–688.

- 26 NIST, NIST: Atomic Spectra Database - Ionization Energies Form, <https://physics.nist.gov/PhysRefData/ASD/ionEnergy.html>, (accessed 2 January 2018).
- 27 T. Makino, H. Kato, S.-G. Ri, Y. Chen and H. Okushi, *Diam. Relat. Mater.*, 2005, **14**, 1995–1998.
- 28 B. Massarani, J. C. Bourgoin and R. M. Chrenko, *Phys. Rev. B*, 1978, **17**, 1758–1769.
- 29 J. Mort, D. Kuhman, M. Machonkin, M. Morgan, F. Jansen, K. Okumura, Y. M. Legrice and R. J. Nemanich, *Cit. Appl. Phys. Lett. Appl. Phys. Lett. J. Appl. Phys. J. Appl. Phys. Appl. Phys. Lett. Appl. Phys. Lett. J. Appl. Phys.*, 1989, **55**, 1121–1695.
- 30 A. T. Collins and A. W. S. Williams, *J. Phys. C Solid State Phys.*, 1971, **4**, 1789–1800.
- 31 R. Samlenski, C. Haug, R. Brenn, C. Wild, R. Locher and P. Koidl, *Diam. Relat. Mater.*, 1996, **5**, 947–951.
- 32 J. Isberg, J. Hammersberg, E. Johansson, T. Wikström, D. J. Twitchen, A. J. Whitehead, S. E. Coe and G. A. Scarsbrook, *Science (80-. )*, 2002, **297**, 1670–1672.
- 33 B. A. Fox, M. L. Hartsell, D. M. Malta, H. A. Wynands, C.-T. Kao, L. S. Plano, G. J. Tessmer, R. B. Henard, J. S. Holmes, A. J. Tessmer and D. L. Dreifus, *Diam. Relat. Mater.*, 1995, **4**, 622–627.
- 34 C. Jacoboni and L. Reggiani, *Adv. Phys.*, 1979, **28**, 493–553.
- 35 F. Nava, C. Canali, C. Jacoboni, L. Reggiani and S. F. Kozlov, *Solid State Commun.*, 1980, **33**, 475–477.
- 36 G. L. Harris, *Properties of silicon carbide*, IEE, INSPEC, 1995.
- 37 C. Hu, *Berkeley*, 2009, 68.
- 38 T. Fiegenbaum, Semiconductor Junctions | Semiconductor Technology | Electronics Video Lecture, <https://www.allaboutcircuits.com/video-lectures/semiconductor-junctions/>, (accessed 8 January 2018).
- 39 A. J. Bard, A. B. Bocarsly, F. Ren, F. Fan, E. G. Walton, M. S. Wrighton and F.-R. F. Fan, *J. Am. Chem. Soc.*, DOI:10.1021/ja00531a001.
- 40 M. Shur, *Physics of semiconductor Devices*, .
- 41 Z. Zhang and J. T. Yates, *Chem. Rev.*, 2012, **112**, 5520–5551.
- 42 L. Austin and H. Starke, *Ann. Phys.*, 1902, **314**, 271–292.
- 43 G. F. Dionne, *J. Appl. Phys.*, 1975, **46**, 3347–3351.
- 44 H. Bruining, *Physics and applications of secondary electron emission.*, New York :, 1954.
- 45 F. Le Pimpec, F. King, R. E. Kirby and M. Pivi, SLAC.
- 46 C. A. Klein, *J. Appl. Phys.*, 1968, **39**, 2029–2038.
- 47 A. Shih, J. Yater, C. Hor and R. Abrams, *Appl. Surf. Sci.*, 1997, **111**, 251–258.
- 48 A. G. Wright, Hamamatsu Photonics, 3rd edn., 2006.
- 49 C. Hawkins, University of Bristol, 2017.
- 50 S. X. Tao, H. W. Chan, H. Van Der Graaf, H. W. Chan@tudelft, H. W. C. NI and V. NI, DOI:10.3390/ma9121017.
- 51 E. J. Sternglass and G. W. Goetze, *IRE Trans. Nucl. Sci.*, 1962, **9**, 97–102.

- 52 CVD diamond - Research, applications, and challenges, <http://www.thindiamond.com/wp-content/uploads/2015/06/201406-MRS-CVD-Diamond-Research-Applications-and-Challenges.pdf>, (accessed 29 January 2018).
- 53 J. D. Levine, *Surf. Sci.*, 1973, **34**, 90–107.
- 54 J. van der Weide, Z. Zhang, P. K. Baumann, M. G. Wensell, J. Bernholc and R. J. Nemanich, *Phys. Rev. B*, 1994, **50**, 5803–5806.
- 55 S. X. Tao, H. W. Chan, H. Van Der Graaf, H. W. Chan@tudelft, H. W. C. NI and V. NI, , DOI:10.3390/ma9121017.
- 56 Picosecond Timing Project, <http://psec.uchicago.edu/>, (accessed 29 January 2018).
- 57 Y. Bilevych, S. E. Brunner, H. W. Chan, E. Charbon, H. van der Graaf, C. W. Hagen, G. Nützel, S. D. Pinto, V. Prodanović, D. Rotman, F. Santagata, L. Sarro, D. R. Schaart, J. Sinsheimer, J. Smedley, S. Tao and A. M. M. G. Theulings, *Nucl. Instruments Methods Phys. Res. Sect. A Accel. Spectrometers, Detect. Assoc. Equip.*, 2016, **809**, 171–174.
- 58 D. C. Joy, in *Materials Science and Technology*, Wiley-VCH Verlag GmbH & Co. KGaA, Weinheim, Germany, 2006.
- 59 J. Ballutaud, C. Bucher, C. Hollenstein, A. A. Howling, U. Kroll, S. Benagli, A. Shah and A. Buechel, , DOI:10.1016/j.tsf.2004.05.034.
- 60 D. S. Knight and W. B. White, , DOI:10.1557/JMR.1989.0385.
- 61 I. Childres, L. A. Jauregui, W. Park, H. Cao and Y. P. Chen, .
- 62 A. C. Ferrari, *Solid State Commun.*, 2007, **143**, 47–57.
- 63 X. Huang, C. Gao, Y. Han, M. Li, C. He, A. Hao, D. Zhang, C. Yu, G. Zou and Y. Ma, *Cit. Appl. Phys. Lett.*, , DOI:10.1063/1.2748084.
- 64 J. Griffiths, *Anal. Chem.*, 2008, **80**, 7194–7197.
- 65 R. Samlenski, C. Haug, R. Brenn, C. Wild, R. Lecher and P. Koidl, .
- 66 R. Bands, RAMAN DATA AND ANALYSIS Raman Spectroscopy for Analysis and Monitoring, <http://www.horiba.com/fileadmin/uploads/Scientific/Documents/Raman/bands.pdf>, (accessed 31 March 2018).
- 67 M. Bernard, A. Deneuve and P. Muret, *Diam. Relat. Mater.*, 2004, **13**, 282–286.